(12) INTERNATIONAL APPLICATION PUBLISHED UNDER THE PATENT COOPERATION TREATY (PCT)

(19) World Intellectual Property Organization
International Bureau

(43) International Publication Date
27 February 2020 (27.02.2020)

WIPO | PCT

(10) International Publication Number
WO 2020/041575 A1

(51) International Patent Classification:
C25B 1/02 (2006.01) *C25B 11/04* (2006.01)

(21) International Application Number:
PCT/US2019/047675

(22) International Filing Date:
22 August 2019 (22.08.2019)

(25) Filing Language: English

(26) Publication Language: English

(30) Priority Data:
62/721,278 22 August 2018 (22.08.2018) US

(71) Applicant: **THE UNIVERSITY OF NORTH CAROLINA AT GREENSBORO** [US/US]; P.O. Box 26170, Greensboro, NC 27402 (US).

(72) Inventor: **WEI, Jianjun**; 7799 Polar Drive, Oak Ridge, NC 27310 (US).

(74) Agent: **WIMBISH, J., Clinton**; Nexsen Pruet, PLLC, 227 West Trade Street, Suite 1550, Charlotte, NC 28202 (US).

(81) Designated States *(unless otherwise indicated, for every kind of national protection available)*: AE, AG, AL, AM, AO, AT, AU, AZ, BA, BB, BG, BH, BN, BR, BW, BY, BZ, CA, CH, CL, CN, CO, CR, CU, CZ, DE, DJ, DK, DM, DO, DZ, EC, EE, EG, ES, FI, GB, GD, GE, GH, GM, GT, HN, HR, HU, ID, IL, IN, IR, IS, JO, JP, KE, KG, KH, KN, KP, KR, KW, KZ, LA, LC, LK, LR, LS, LU, LY, MA, MD, ME, MG, MK, MN, MW, MX, MY, MZ, NA, NG, NI, NO, NZ, OM, PA, PE, PG, PH, PL, PT, QA, RO, RS, RU, RW, SA, SC, SD, SE, SG, SK, SL, SM, ST, SV, SY, TH, TJ, TM, TN, TR, TT, TZ, UA, UG, US, UZ, VC, VN, ZA, ZM, ZW.

(84) Designated States *(unless otherwise indicated, for every kind of regional protection available)*: ARIPO (BW, GH, GM, KE, LR, LS, MW, MZ, NA, RW, SD, SL, ST, SZ, TZ, UG, ZM, ZW), Eurasian (AM, AZ, BY, KG, KZ, RU, TJ, TM), European (AL, AT, BE, BG, CH, CY, CZ, DE, DK, EE, ES, FI, FR, GB, GR, HR, HU, IE, IS, IT, LT, LU, LV, MC, MK, MT, NL, NO, PL, PT, RO, RS, SE, SI, SK, SM, TR), OAPI (BF, BJ, CF, CG, CI, CM, GA, GN, GQ, GW, KM, ML, MR, NE, SN, TD, TG).

Published:
— *with international search report (Art. 21(3))*

(54) Title: COMPOSITIONS AND METHODS FOR ENHANCING ELECTROCATALYTIC EFFICIENCIES

(57) Abstract: A method of enhancing efficiency of an oxygen evolution reaction (OER), oxygen reduction reaction (ORR), or hydrogen evolution reaction (HER) comprises increasing total number electron pathway and/or reaction kinetics of the OER, ORR, or HER by coating one or more surfaces of an electrode participating in the OER, ORR, or HER with one or more metal oxides.

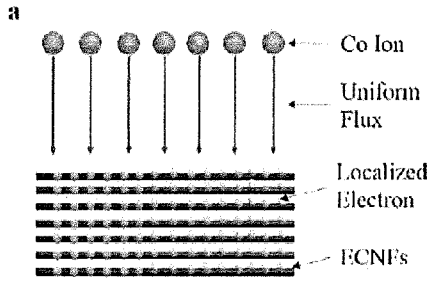

FIG. 3

WO 2020/041575 A1

COMPOSITIONS AND METHODS FOR ENHANCING ELECTROCATALYTIC EFFICIENCIES

RELATED APPLICATION DATA

The present application claims priority pursuant to 35 U.S.C. § 199(e) to United States Provisional Patent Application Serial Number 62/721,278 filed August 22, 2018, which is incorporated herein by reference in its entirety.

FIELD

The invention generally relates to compositions and methods for conducting electrocatalytic reactions and, in particular, to compositions and methods for enhancing electrocatalytic efficiencies.

BACKGROUND

Given the promise shown by electrochemical cells as devices for generating clean and sustainable energy, the electrocatalytic oxygen reduction reaction (ORR) or hydrogen evolution reaction (HER) has been widely studied using steady-state polarization, rotating disk electrodes (RDE), rotating ring-disk electrodes (RRDE), and cyclic voltammetry. Electrocatalysts including carbon-based materials, such as glassy carbon (GC), graphite, activated carbon, and carbon nanotubes; Pt catalysts (Pt nanoparticles and Pt alloys); and transition metal-based catalyst (cobalt and iron) have been explored for conducting the ORR. ORR or HER performance is complex, varying with synthesis conditions, nitrogen doping, metal type, and pyrolysis temperature. For ORR, to ensure that the fuel cell generates the maximum power output, a 4-electron pathway (from oxygen to water) is necessary, because the 2-electron pathway (from oxygen to hydrogen peroxide) involved in the cathodic process dramatically compromises the energy yield of the fuel cell. Moreover, cell membranes and other supporting materials are impaired by the presence of excess hydrogen peroxide, owing to peroxide radicals generated from a disproportionation reaction.

Consequently, improved methods for increasing and maintaining the efficiency of the 4-electron pathway are needed.

SUMMARY

In one aspect, methods of enhancing efficiency of an oxygen evolution reaction (OER), oxygen reduction reaction (ORR), or hydrogen evolution reaction (HER) are described herein which, in some embodiments, can provide one or more advantages compared to other methods. In some embodiments, a method of enhancing efficiency of an oxygen evolution reaction (OER), oxygen reduction reaction (ORR) and/or hydrogen evolution reaction (HER) comprises increasing total number electron pathway and reaction kinetics of the OER, ORR or HER by coating one or more surfaces of an electrode participating in the OER, ORR or HER with one or more metal oxides.

Metal(s) of the oxide coating can comprise one or more transition metals, non-transition metals or various combinations thereof. In some embodiments, metal of the oxide or transition metal of the oxide is paramagnetic. Suitable transition metals of the oxide, for example, can be selected from Groups IIIB-VIIIB of the Periodic Table. In some instances, the metal oxide comprises manganese oxide, iron oxide, and/or cobalt oxide. The metal oxide can also comprise one or more dopants. The dopants can include one or more alkali metals, alkaline earth metals or mixtures thereof.

In some embodiments, the coating comprising metal oxide has structure to confine reaction products created at the electrode, where one or more of the reaction products undergo oxidation or reduction by the electrode.

The metal oxide can be deposited on any part and/or composition of the electrode not inconsistent with the objectives of the present invention. In some embodiments, for example, the metal oxide is deposited one or more carbon nanostructures of the electrode. These carbon nanostructures can comprise nanofibers, nanotubes, nanospheres, nanosheets, graphene, nanodots or combinations thereof. In some instances, the carbon nanostructures are aligned carbon nanofibers.

As described further herein, the metal oxide coating can increase the total number electron pathway and/or reaction kinetics of the OER, ORR and/or HER. In some embodiments, for example, the total number electron pathway of the ORR can be at least 3.4. In other embodiments, the total number electron pathway can range from 3.6 to 4, 3.85 to 4 or 3.9 to 4.

Notably, methods described herein can further comprise applying a magnetic field to the metal oxide coated electrode, where the applied magnetic field has a magnitude of 0.1 to 1000 mT.

In another aspect, a method of enhancing efficiency of an oxygen evolution reaction (OER), oxygen reduction reaction (ORR), and/or hydrogen evolution reaction (HER) comprises increasing total number electron pathway and/or reaction kinetics by conducting the OER, ORR and/or HER in an applied magnetic field. In some embodiments, the applied magnetic field has a magnitude of 0.1 to 1000 mT. The total number electron pathway of the ORR conducted under the applied magnetic field can be at least 3.4 or at least 3.6. In some embodiments, the total electron pathway for the ORR can range from 3.85 to 4 or 3.9 to 4.

One or more electrodes participating in the OER, ORR or HER can have any construction and/or properties described herein. An electrode, for example, can comprise a metal oxide coating as described above. Additionally, the metal oxide coating can have structure to confine reaction products created at the electrode, were the one or more of the reaction products undergo oxidation or reduction by the electrode.

In another aspect, an energy generation device comprises an electrochemical cell comprising one or more electrodes for performing an oxygen evolution reaction (OER), oxygen reduction reaction (ORR), or hydrogen evolution reaction (HER); and a magnetic field source for application of a magnetic field to the one or more electrodes during the OER, ORR or HER.

These and other embodiments are further described in the detailed description, which follows.

BRIEF DESCRIPTION OF THE DRAWINGS

Figures 1a-1h are scanning electron microscopy ("SEM") images of well-aligned ECNFs (Figure 1a) and Co_3O_4/ECNFs for electrodeposition times of 1–8 h (Figures 1b–1h, respectively) with the histograms (y axis is the frequency) of size distribution analysis;

Figure 2a is a SEM image associated with energy-dispersive x-ray (EDX) mapping analysis of the Co_3O_4/ECNFs under electrodeposition of 5 h;

Figure 2b is an FTIR spectrum of Co_3O_4/ECNFs under electrodeposition of 1h-8h;

Figure 2c is a Raman spectrum of Co_3O_4/ECNFs under electrodeposition of 1h-8h;

Figure 2d is XRD analysis of the Co_3O_4/ECNFs under electrodeposition times of 1h-8h;

Figure 3a is a schematic representation of Co^{2+} uniform flux;

Figure 3b is a graphical representation of time-dependent Co_3O_4 growth;

Figure 3c is a schematic representation of a Co_3O_4 growth mechanism;

Figure 4a is a graphical representation of a time-dependent exchanged electron number (n) of the ORR at an electrode modified with Co_3O_4/ECNFs in O_2-saturated 20 mm KCl electrolyte solution;

Figure 4b is a graphical representation of an electrochemical impedance spectroscopy at frequencies from 100 kHz to 0.1 kHz;

Figure 5a is a schematic representation of an exemplary magnetic field setup;

Figure 5b is a graphical representation of a linear dependence of the log of a peak current on the potential for a transfer coefficient calculation;

Figure 5c is a graphical representation of a linear dependence of a peak current on a square root of a scan rate for an exchanged electron number calculation;

Figure 5d is a graphical representation of a dependence of an exchanged electron number (n) on a magnetic field applied to the ORR at a GC electrode modified with Co3O4/ECNFs (5 h electrodeposition);

Figure 6a is a graphical representation of dependence of a peak potential on a scan rate under different magnetic fields of the ORR with an electrode modified with Co_3O_4/ECNFs (5 h electrodeposition);

Figure 6b is a graphical representation of $\ln(k_m/k_0)$ of oxygen reduction versus magnetic field for the electrode modified with Co_3O_4/ECNFs with linear fit;

Figure 7a is a graphical representation of dependence of a peak potential shift on a scan rate under different magnetic fields regarding the electron transfer kinetics of a Co_3O_4 electrode system.

Figure 7b is a schematic representation of the effects of magnetic field effects on an electronic configuration;

Figure 7c is a graphical representation of $\ln(k_m/k_0)$ versus magnetic field with linear fit regarding the electron transfer kinetics of a Co_3O_4 electrode system;

Figure 7d is a schematic representation of a mechanism of a magnetically enhanced 4-electron pathway;

Figure 8 is a schematic representation of an aligned electrospinning technique and device;

Figure 9 is a cyclic voltammogram of the ORR at a bare glassy carbon electrode;

Figure 10 is a cyclic voltammograms of the ORR at a Co_3O_4/ECNFs modified electrode;

Figure 11 is a cyclic voltammogram of a H_2O_2 reduction reaction at a Co_3O_4/ECNFs modified electrode;

Figure 12 is a cyclic voltammogram of a H_2O_2 reduction reaction at a bare glassy carbon electrode and an ECNFs-modified GC electrode;

Figures 13a-13f are scanning electron microscopy ("SEM") images of well-aligned ECNFs (Figures 13a and 13b) and MnO_2/ECNFs for electrodeposition times of 2h and 4h (Figures 13c/13d and 13e/13f, respectively) with the histograms (y axis is the frequency) of size distribution analysis;

Figure 14a-14f are characterization of super-aligned ECNFs and MnO2/ECNFs after 4h electrodeposition time, where Figure 14a is a SEM associated with EDX mapping analysis, Figure 14b is thermogravimetric analysis (TGA), Figure 14c is Raman spectrum analysis, Figure 14d is Fourier transform infrared (FTIR) spectrum analysis, Figure 14e is x-ray photoelectron spectroscopy (XPS) spectrum analysis, and Figure 14f is x-ray diffraction (XRD) analysis;

Figure 15a is cyclic voltammograms of the ORR at a bare glassy carbon electrode in O_2 saturated 20 mM KCl electrolyte solution at different scan rates;

Figure 15b is a graphical representation of linear dependence of the peak current on the square root of the voltage scan rate for an O_2 concentration calculation;

Figure 16a is a cyclic voltammograms of the ORR at an electrode modified with super-aligned ECNFs;

Figure 16b is a cyclic voltammograms of the ORR at an electrode modified with MnO_2/ECNFs (4 h electrodeposition) in O_2 saturated 20 mM KCl electrolyte solution at different scan rates;

Figure 16c is a graphical representation of a linear dependence of the peak current on the square root of the scan rate for the number of electrons exchanged calculation for an electrode modified with MnO_2/ECNFs (4 h electrodeposition);

Figure 16d is a graphical representation of a linear dependence of the log of the peak current on the potential for the transfer coefficient calculation for an electrode modified with MnO_2/ECNFs (4 h electrodeposition);

Figure 17a is a cyclic voltammograms of the H_2O_2 reduction reaction at the electrode modified with MnO_2/ECNFs (4 h) in N_2 saturated 20 mM KCl electrolyte solution with 1 mM H_2O_2 at different scan rates;

Figure 17b is a graphical representation of linear dependence of the peak current on the square root of the scan rate for the number of electrons exchanged calculation, inserted with the linear dependence of the log of the peak current on the potential for a transfer coefficient calculation;

Figure 18 is a graphical representation of peak potential versus log of scan rate for critical scan rate determination under the conditions of H_2O_2-MnO_2 and O_2-ECNFs;

Figure 19 is a schematic representation of a 4-electron pathway mechanism by the bifunctional catalyst α-MnO_2/ECNFs-GC electrode; and

Figure 20 is a schematic representation of a method of uniform electrodeposition of MnO_2 on super-aligned ECNFs.

Fig. 21a illustrates OER current densities for MnO_2 coated ECNFs fabricated according to methods described herein under applied magnetic fields of varying strength, according to some embodiments.

Fig. 21b illustrates OER current densities for MnO_2 coated ECNFs in the absence of magnetic field application, according to some embodiments.

Fig. 22a illustrates OER current densities for the Fe_2O_3 coated ECNFs under application of magnetic fields of varying strength, according to some embodiments.

Fig. 22b illustrates OER current densities for the Fe_2O_3 coated ECNFs in the absence of magnetic field application, according to some embodiments.

Fig. 23 is a SEM of the Fe_2O_3-MnO_2 coated ECNFs, according to some embodiments.

Fig. 24a illustrates OER current densities for the Fe_2O_3-MnO_2 coated ECNFs under application of magnetic fields of varying strength, according to some embodiments.

Fig. 24b illustrates OER current densities for the Fe_2O_3-MnO_2 coated ECNFs in the absence of magnetic field application, according to some embodiments.

Fig. 24c is a Tafel plot illustrating increased OER efficiencies of the Fe_2O_3-MnO_2 coated ECNFs with increasing magnetic field strength, according to some embodiments.

DETAILED DESCRIPTION

Embodiments described herein can be understood more readily by reference to the following detailed description and examples. Elements, apparatus and methods described herein, however, are not limited to the specific embodiments presented in the detailed description and examples. It should be recognized that these embodiments are merely illustrative of the principles of the present invention. Numerous modifications and adaptations will be readily apparent to those of skill in the art without departing from the spirit and scope of the invention.

In addition, all ranges disclosed herein are to be understood to encompass any and all subranges subsumed therein. For example, a stated range of "1.0 to 10.0" should be considered to include any and all subranges beginning with a minimum value of 1.0 or more and ending with a maximum value of 10.0 or less, e.g., 1.0 to 5.3, or 4.7 to 10.0, or 3.6 to 7.9. Similarly, a stated range of "1 to 10" should be considered to include any and all subranges beginning with a minimum value of 1 or more and ending with a maximum value of 10 or less, e.g., 1 to 5, or 4 to 10, or 3 to 7, or 5 to 8.

All ranges disclosed herein are also to be considered to include the end points of the range, unless expressly stated otherwise. For example, a range of "between 5 and 10" or "from 5 to 10" or "5-10" should generally be considered to include the end points 5 and 10.

Further, when the phrase "up to" is used in connection with an amount or quantity, it is to be understood that the amount is at least a detectable amount or quantity. For example, a material present in an amount "up to" a specified amount can be present from a detectable amount and up to and including the specified amount.

In one aspect, a method of enhancing efficiency of an oxygen evolution reaction (OER), oxygen reduction reaction (ORR) and/or hydrogen evolution reaction (HER) comprises increasing total number electron pathway of the OER, ORR and/or HER by coating one or more surfaces of an electrode participating in the OER, ORR, or HER with one or more metal oxides.

In another aspect, a method of enhancing efficiency and/or reaction kinetics of an OER, ORR, or HER comprises increasing a total number electron pathway of the OER by conducting the OER, ORR, or HER in an applied magnetic field. In some instances, the applied magnetic field enhances the electrocatalytic efficiency of a transition metal oxide.

In some embodiments, methods described herein can be used for catalyzing OER, ORR, and/or HER in fuel cell, metal-air batteries, and electrochemical cell for water splitting. For

example, the methods can enhance an electron transfer rate (kinetics) of the 4-electron pathway in ORR using a paramagnetic transition metal oxide electrocatalyst.

In some embodiments, methods described herein comprise depositing one or more transition metal oxides on an electrode scaffold; applying a magnetic field to the deposited transition metal oxide, and conducting an electrocatalytic reaction with the deposited transition metal oxide in the presence of the magnetic field. Non-limiting examples of metal oxides comprise MnO_2, Co_3O_4, Fe_2O_3, Fe_3O_4, TiO_2, NiO_x, and various combinations thereof. The efficiency of the electrocatalytic reaction can be enhanced by the presence of the magnetic field by improving electron or charge transportation when metal oxides or composites are used for electrocatalysis. In some instances, the electrocatalytic reaction efficiency enhancement occurs under milli-tesla (mT) to tesla strength of magnetic field.

The electrode scaffold can comprise a carbon material, a nanostructured carbon material (i.e. carbon nanostructures), a metal substrate, or other types of electrode scaffolding materials. The carbon material can comprise graphite or other similar carbon-based materials. The nanostructured carbon material can comprise carbon nanotubes, carbon nanofibers, graphene, nanospheres, nanodots, graphene nanofoam (GF), or a reduced graphene oxide (rGO) scaffold. Any other type of nanostructured carbon material not inconsistent with the instant disclosure can be fabricated and used as a scaffold for transition metal oxides. In some embodiments, the electrode scaffold comprise nitrogen-doped electrospun carbon nanofibers (ECNFs). These ECNFs can be produced by carbonizing electrospun polyacrylonitrile (PAN). These nitrogen-doped ECNFs also in some embodiments serve as an electrocatalyst for the ORR in some instances. Aligned ECNF structures can be used as scaffolds to uniformly support metal oxide nanostructures, because their alignment enhances the deposition rate by shortening the distance for electron transport.

In an embodiment, the transition metal oxide is selected from Groups IIIB-VIIIB of the Periodic Table. In some instances, the transition metal oxide is Co_3O_4. Co_3O_4, which incorporates mixed-valence Co^{2+} and Co^{3+}. Co_3O_4 has magnetically susceptibility, owing to its spin/spin–orbit coupling-induced magnetic moment, and, as described herein, an external magnetic field affects the electrochemical performance of Co_3O_4 as an electrocatalyst. In other instances, the transition metal oxide is MnO_2, Fe_2O_3, Fe_3O_4, TiO_2, NiO_x, or various combinations thereof, which also have magnetic susceptibility owing to their respects spin/spin–orbit coupling-

induced magnetic moments, through which an external magnetic field affects their electrochemical performances as electrocatalysts. Accordingly, while the remaining descriptions herein describe various embodiments using MnO_2, Fe_2O_3 and/or Co_3O_4 as examples, it is to be understood that such embodiments equally apply to, and include, embodiments where the transition metal oxide is Fe_3O_4, TiO_2, NiO_x, or other similar transition metal oxides in Groups IIIB-VIIIB.

In an embodiment, the transition metal oxide comprises MnO_2, Fe_2O_3 and/or Co_3O_4, and the electrode scaffolding material comprises ECNFs. Thus, in some instances, the method comprises depositing MnO_2, Fe_2O_3, and/or Co_3O_4 on a surface of the ECNFs. In some embodiments, more than one metal oxide is deposited on a surface of the ECNFs. The MnO_2 can be electrodeposited at the surface of the ECNFs to form MnO_2/ECNFs. Likewise, Co_3O_4 can be electrodeposited at the surface of the ECNFs to form Co_3O_4/ECNFs. In some embodiments, MnO_2 and Fe_2O_3 are co-deposited at the surface of ECNFs to form MnO_2–Fe_2O_3/ECNFs. When two or more metal oxides are deposited, each metal oxide can be uniformly dispersed in the coating. Alternatively, metal oxides of the coating may be heterogeneously distributed in the coating.

As described in more detail below, an electron transfer reaction of MnO_2 and catalytic ORR reactions have been carried out using uniform electrodepositions of α-MnO_2 on ECNFs. In some embodiments, the MnO_2/ECNFs composite formed by the method described herein, demonstrates a 3.84 electron pathway. As a reference, the theoretical number of electron pathway is 4 for oxygen reduction to water, indicating a large cycle number and excellent catalytic activity obtained by uniform electrodeposition of α-MnO_2 on ECNFs. In other embodiments, the MnO_2/ECNFs composite has an electron pathway of at least 3.7, at least 3.8, at least 3.9, or more than 3.9.

Additionally described below, an electron transfer reaction of Co_3O_4 and catalytic ORR reactions have been carried out in the presence and absence of a magnetic field. In some embodiments, a rate of charge transportation for the number of electron pathways and/or reaction kinetics of ORR (representing the efficiency or ORR complete) increases monotonically in the presence of an applied magnetic field having a strength in a range of 0-1.32 mT. In some instances the rate of charge transportation increases monotonically with a magnetic field strength of 0-1.40mT, 0-1.50mT, 0-1.60mT, 0-1.7mT, 0-1.8mT, 0-1.9mT, or 0-2.0mT. In some

embodiments, the Co_3O_4/ECNFs composite formed by the method described herein, demonstrates a 3.92 electron pathway in the presence of a 1.32 mT magnetic field, in contrast to a 3.48 electron pathway in the absence of a magnetic field. In other embodiments, the Co_3O_4/ECNFs composite has an electron pathway of at least 3.5, at least 3.6, at least 3.7, at least 3.8, or at least 3.95 in the presence of a 1.32 mT magnetic field.

In further embodiments, OER reactions have been carried out using depositions of Fe_2O_3 on ECNFs and Fe_2O_3–MnO_2 composites on ECNFs. These OER reactions were carried out in the presence and absence of magnetic fields of varying strengths.

I. Fabrication of ECNFs

In one aspect, a fabrication method for well-aligned ECNFs is described. In some embodiments, the method comprises fabricating a plurality of interconnected carbon nanofibers via electrospinning. In some embodiments, electrospinning includes spinning a polyacrylonitrile (PAN) on a collector to form a fiber fabric and then pressing and carbonizing the fabric. Other electrospinning techniques can also be used and/or provided.

The ECNFs have reasonably electrical conductive cores (e.g., having a conductivity: 1~10 S/cm) that support and utilize electro-active MnO_2 or Co_3O_4 coatings. Moreover, ECNFs provide an excellent mechanical scaffold with porosity and interconnectivity for superior hybrid structure.

ECNFs are but one embodiment of the carbon nanostructures that can be used to form electrodes for energy storage devices described herein. However, electrospinning is not required. Other carbon nanostructures can be fabricated according to different fabrication techniques and used as electrode scaffolds for transition metal oxides. Such nanostructures can include carbon nanotubes, carbon nanofibers, graphene, nanospheres, nanodots, graphene nanofoam (GF), or a reduced graphene oxide (rGO) scaffold. Any other type of carbon nanostructure not inconsistent with the instant disclosure can be fabricated and used as a scaffold for metal oxides or transition metal oxides, such as MnO_2 or Co_3O_4.

In some instances, fabrication of well-aligned ECNFs comprises a facile electrospinning method with a self-designed sample collector, as shown for example in Figure 8. Different from a normal cylinder design, four steel poles were welded onto a plate to collect the ECNFs without any substrate. After carbonization, the as-prepared pure ECNFs exhibit a well aligned structure

(Figures 1a and 13a). A nitric acid pretreatment, which introduces hydroxy and carboxyl groups, can be used to make the ECNFs surface more hydrophilic and to introduce reaction sites for the nucleation of MnO_2 or Co_3O_4 crystallites.

II. Co_3O_4 Growth Characterization and Mechanism

Fabrication methods for Co_3O_4 electrodeposition onto the well-aligned ECNFs is described herein, where Co_3O_4 electrodeposition onto the ECNFs forms a uniform, dense film of Co_3O_4 having a self-limiting thickness.

In this embodiment, a uniform layer of the transition metal oxide, Co_3O_4, can be electrodeposited on each of the plurality of ECNFs. The transition metal oxide can include Co_3O_4 that is electrodeposited on each of the plurality of ECNFs, although any other metal oxide or transition metal oxide not inconsistent with the goals of this disclosure can also be electrodeposited. In some embodiments, low current electrodeposition techniques are used to grow a fine and firm layer of the metal oxide (e.g., Co_3O_4). The aforementioned fabrication processes (i.e., electrospinning and electrodeposition) are facial and scalable.

In some instances, a constant low current (50 mA) can applied for the electrodeposition by an electrochemical workstation for various times ranging from 1 h to 8 h under an N_2 atmosphere with an aqueous precursor solution containing 20 mM Co_3O_4 and 100 mM Na_2SO_4. The composites' structures and morphologies were characterized by scanning electron microscopy (SEM; Figures 1b-1h). When the electrodeposition starts, thin films form on the functionalized sites distributed on the fibers (Figures 1b and 1c). As electrodeposition continues, the films begin to grow denser/thicker and the fibers are fully covered (Figures 1d and 1e). After electrodeposition for 5 h, ECNFs with a nanofiber diameter of about 206 nm are decorated by a Co_3O_4 film with a thickness of about 797 nm, making a total diameter of about 1003 nm (Figure 1f). Co_3O_4 electrodeposition beyond a 5 h time does not show an obvious thickness increase with the applied constant current (Figures 1g and 1h), a feature of self-cessation that likely arises from the increased resistance of the Co_3O_4 layers and low current for electrodeposition.

The chemical composition of the composites under different electrodeposition times from 1 h to 8 h was analyzed by energy-dispersive X-ray (EDX) spectroscopy, Raman spectroscopy, and Fourier transform infrared spectroscopy (FTIR). The EDX spectra (Figure 2a) show that the surface composition of the electrochemically deposited electrodes is composed of the elements

C, O, and Co. The peaks observed at 567 and 668 cm^{-1} in the FTIR spectrum correspond to the stretching vibrations of metal oxide for tetrahedrally coordinated Co^{2+} and octahedrally coordinated Co^{3+} (Figure 2b), which is further verified by the Raman shifts of 510 and 682 cm^{-1} (Figure 2c).

The Co_3O_4 crystal structure was determined for the as-prepared Co_3O_4/ECNFs materials using X-ray diffraction (XRD; Figure 2d). The comprehensive electrodeposition of Co_3O_4 originates from the stable structure of ECNFs, which contributes to a uniform Co^{2+} flux (Figure 3a). The electrochemical reaction occurs according to Equation (1):

$$3\,CO^{2+} + 4\,H_2O \rightarrow CO_3O_4 + 8\,H^{+} + 2\,e^{-} \qquad \textbf{Eq. 1}$$

In this growth process, the thickness of the Co_3O_4 film can be controlled by the electrodeposition time (Figure 3b). The growth of the metal oxide film can be analyzed by controlled current electrodeposition kinetics. A general three-step growth model has been derived according to the measured results, and the Co_3O_4 thickness (h) versus deposition time (t) has a best fit as follows (Equation (2)):

$$h = h_{max}/(1 + 10^{(\tau_{0.5} - t)})(t > 0) \qquad \textbf{Eq. 2}$$

with $h_{max} \approx 851$ nm and the half-life time constant $\tau_{0.5} \approx 3.59$ h. The time-dependent growth analysis in some instances describes a three-step kinetics mechanism for the electrodeposition (Figure 3c). The first step involves thin film formation on a boundary layer distributed along the fibers (0–2 h). The second step involves dense film formation and the ECNFs are fully covered (2–5 h). The last step involves the cessation of Co_3O_4 growth and the establishment of a uniform, dense film with a self-limiting thickness (>5 h).

III. Co_3O_4 Thickness-Dependent Electron Pathway

In an aspect, an increase of Co_3O_4 thickness (1–5 h electrodeposition) also increases the number of exchanged electrons (n). The increase in the number of exchanged electrons (n) is due to oxygen and hydrogen peroxide being effectively confined within the aligned Co_3O_4/ECNFs system. In some embodiments, hydrogen peroxide molecules generated from a electrochemical

reduction of oxygen can be decomposed repeatedly at the surface of a uniform Co_3O_4 film formed within an aligned Co_3O_4/ECNFs system.

The ORR activity was determined through cyclic voltammetric responses of a bare GC electrode. For example, Figure 9 shows cyclic voltammograms of the ORR at a bare glassy carbon electrode in O_2 saturated 20 mM KCl electrolyte solution at scan rates of 10-70 mV s^{-1}. The cathodic peak results from the electrochemical reduction of oxygen and the magnitude of the cathodic peaks increases with increasing voltage scan rates. The Butler–Volmer model can be used to describe the electrochemical kinetics of the ORR process. In this case, the slope (slope 1) of a plot of log(peak current) versus peak potential (E_p [V]) and Equation (3) are used to determine the transfer coefficient (a):

$$\text{Slope 1} = \frac{-\alpha F}{2.3RT} \qquad \textbf{Eq. 3}$$

where R is the gas constant, F is the Faraday constant, and T is the temperature. In addition, the peak current, i_p [A], is measured as a function of the square root of the voltage scan rate (v[Vs^{-1}]). The slope (slope 2) can be used to characterize the concentration of oxygen in the bulk solution (C [mol mL^{-1}]) through Randles–Sevcik equation:

$$|\text{Slope 2}| = (2.99 \times 10^5)\, n^{3/2} \alpha^{1/2} A C D_0^{1/2} \qquad \textbf{Eq. 4}$$

where n is the exchanged electron number during the electrochemical process (n=2 at a bare GC electrode), A is the active surface area of the bare GC electrode (0.071 cm2), D_0 is the diffusion coefficient (1.95×10^{-5} cm^2 s^{-1}). When the above constants are applied to an absolute value of slope 2 (obtained from Figure S4), the oxygen concentration of 2.50×10^{-7} mol mL^{-1} can be derived. Changing the range of potential scan rate does not affect the magnitudes of slopes 1 and 2.

The cyclic voltammetric responses of the ORR at the Co_3O_4/ECNFs-modified electrode (1–8h electrodeposition) were examined to find the number of exchanged electrons. The cyclic voltammograms show an increase in the cathodic peak current (at about -0.5 V) with respect to the scan rate (Figure 10). The cathodic peak presented at about 0.60 V is attributed to the reduction reactions between the Co^{III}/Co^{II} complexes. As described above, Equations (3) and (4) are also used to calculate the number of exchanged electrons in the overall electrochemical

processes for electrodes modified with Co_3O_4/ECNFs (1-8 h electrodeposition). The numbers of exchanged electrons were found to be 3.09, 3.27, 3.36, 3.43, 3.48, 3.46, and 3.42 for the Co_3O_4/ECNFs modified electrodes under electrodeposition times of 1, 2, 3, 4, 5, 6, and 8 h, respectively, as shown in Table 1.

Table 1

Time	Slope 1	Slope 2	n
1 h	-1.32±0.11	$(-3.56\pm0.07)\times10^{-5}$	3.09±0.14
2 h	-1.43±0.02	$(-4.03\pm0.12)\times10^{-5}$	3.27±0.09
3 h	-1.61±0.05	$(-4.46\pm0.10)\times10^{-5}$	3.36±0.12
4 h	-1.77±0.04	$(-4.81\pm0.05)\times10^{-5}$	3.43±0.07
5 h	-2.10±0.08	$(-5.36\pm0.04)\times10^{-5}$	3.48±0.06
6 h	-1.96±0.06	$(-5.13\pm0.02)\times10^{-5}$	3.46±0.03
8 h	-1.94±0.06	$(-5.02\pm0.07)\times10^{-5}$	3.42±0.08

Figure 11 shows the cyclic voltammogram of a Co_3O_4/ECNFs-modified electrode in an N_2-saturated 20 mm KCl electrolyte solution containing 1 mm hydrogen peroxide at different scan rates. No measurable reduction peak is observed for either a bare GC electrode or an ECNFs-modified GC electrode in the same solution (Figure 12), so a marked increase in the reduction current at the voltage of the Co_3O_4/ECNFs-modified electrode (-0.5 V vs. Ag/AgCl in Figure S9) results from the electrochemical decomposition of hydrogen peroxide taking place at the electrode surface. In some instances, the hydrogen peroxide molecule generated from the electrochemical reduction of oxygen can be decomposed repeatedly at the surface of a uniform Co_3O_4 film. Moreover, a 4-electron pathway can have a cycle of oxygen decomposition and regeneration using a Co_3O_4/ECNFs-modified electrode. Therefore, in some embodiments, with an increase of Co_3O_4 thickness (1–5 h electrodeposition), the number of exchanged electrons (n) increases owing to oxygen and hydrogen peroxide being effectively confined within the aligned Co_3O_4/ECNFs system (Figure 4a).

Although there is no obvious thickness difference for Co_3O_4 electrodeposition beyond 5 h in time, a decreased n for Co_3O_4/ECNFs electrodes is observed with 6 h (charge transfer

resistance &137 W) and 8 h (charge transfer resistance ≈ 149 Ω) electrodeposition, likely due to resistance increases. When the electrodeposition time is longer than 5 h, the longer electrodeposition results in a more compact Co_3O_4/ECNFs composite (i.e., higher density), causing the internal resistance increase, whereas the apparent thickness of the Co_3O_4 film on single ECNF undergoes no obvious change. The resistance was deduced from electrochemical impedance spectroscopy (EIS) Nyquist plots (Figure 4b) and fitting a Randles circuit model.

IV. Magnetically enhanced electron transfer (MEET)

According to further aspects, magnetic field polarization on unpaired electron spin of Co_3O_4 enhances the kinetics of a Co^{III}/Co^{II} redox reaction in Co_3O_4/ECNFs catalytic centers. The magnetic field polarization can in some embodiments, advantageously enhance the energy storage capabilities. Furthermore, in such embodiments, coupling of the Co^{III}/Co^{II} redox reaction and the ORR process facilitates a faster rate of oxygen reduction by the Co_3O_4/ECNFs to fulfill a nearly 4-electron pathway during the oxygen reduction reaction process. In certain embodiments, the magnetic field provided while charging the supercapacitor is 0.1- 0.5 mT, 0.1-1 mT, 0.1-2 mT, 0.1-5 mT, 1-2 mT, or 1-5 mT or higher.

The cyclic voltammetric responses of the Co_3O_4/ECNFs (5 h electrodeposition) modified electrode for ORR were examined under different magnetic fields (Figure 5a). According to slope 1 [Eq. (3)] from a plot of log (peak current) versus potential (Figure 5b) and slope 2 [Eq. (4)] from the peak current position on the square root of the voltage scan rate (Figure 5c), in some embodiments an increased number of exchanged electrons were obtained for the Co_3O_4/ECNFs-modified electrodes under magnetic fields of 0.22, 0.44, 0.66, 0.88 mT, 1.10 mT, 1.32 mT (Figure 5d, Table 2).

Table 2

Magnetic field (mT)	Slope 1	Slope 2	n
0.00	-2.10 ± 0.08	$(-5.36 \pm 0.04) \times 10^{-5}$	3.48 ± 0.06
0.22	-2.12 ± 0.14	$(-5.78 \pm 0.13) \times 10^{-5}$	3.65 ± 0.13
0.44	-2.14 ± 0.17	$(-6.08 \pm 0.14) \times 10^{-5}$	3.76 ± 0.15
0.66	-2.19 ± 0.12	$(-6.31 \pm 0.19) \times 10^{-5}$	3.82 ± 0.14
0.88	-2.20 ± 0.11	$(-6.44 \pm 0.24) \times 10^{-5}$	3.87 ± 0.16
1.10	-2.25 ± 0.13	$(-6.56 \pm 0.18) \times 10^{-5}$	3.89 ± 0.14
1.32	-2.28 ± 0.12	$(-6.67 \pm 0.17) \times 10^{-5}$	3.92 ± 0.13

Dependence of the number of exchanged electrons on the magnetic field of the ORR at the electrode modified with Co_3O_4/ECNFs (5h electrodeposition).

There is no measurable difference in the number of electrons exchanged on the bare GC electrode in absence or presence of an external magnetic field at 1.32 mT. Therefore, an external mT-range magnetic field by itself does not have an effect on oxygen diffusion/transfer due to the applied magnetic field strength. A small difference in this number was observed for the ECNFs-modified electrode in the absence ($n \approx 2.28$) and presence ($n \approx 2.35$, 3.1% increase) of an external magnetic field at 1.32 mT, indicating that the external mT-range magnetic field can promote the transfer of paramagnetic peroxo radicals along the porous structure of the ECNFs as a result of the Lorentz force. However, in embodiments having the hybrid of Co_3O_4 with ECNFs much greater activity (n=3.48 vs. 2.28 at 0 mT) is observed when the external mT-range magnetic field is applied. In other embodiments, Co_3O_4 is supported on graphene or carbon nanotubes and has similar increases in activity as Co_3O_4/ECNFs. Consequently, the difference (n=3.92 at 1.32 mT vs. 3.48 at 0 mT, corresponding to an increase of 12.6%) in the number of electrons exchanged in the ORR pathway at the hybrid Co_3O_4/ECNFs-modified electrode is mainly a result of the magnetic field effect on the Co_3O_4 film. Moreover, the magnitude of slope 1 increases with the increase of magnetic field strength (Table 2), due to the occurrence of magnetically enhanced electron transfer (MEET) reactions. Cyclic voltammetry is a tool to probe the electrochemical kinetics of a redox reaction in solution by an electrode. The heterogeneous rate constant can be derived as a function of the shift in observed reduction peak with the scan rate. The established model was used to estimate the heterogeneous electron-transfer rate constant during the ORR process (k^0_{ORR} [cm s^{-1}]):

$$k^0_{ORR} = 2.18\left(\frac{\alpha D_0 nFv}{RT}\right)\exp\left(\frac{-2\alpha^2 nF(E_0 - E_p)}{RT}\right) \qquad \textbf{Eq. 5}$$

where E_0 is the formal potential determined by the y intercept at a scan rate of 0 mVs^{-1} (Figure 6a), E_p is the peak potential at scan rate v, and other parameters are the same as mentioned above. By using the experimental results at different scan rates (20 mVs^{-1} in Table 3 as an example) combined with the transfer coefficient, number of electrons exchanged, and diffusion coefficient obtained above, the values of heterogeneous electron transfer rate constant are calculated (Table 3):

Table 3

Magnetic field (mT)	E_0 (V)	E_p (V)	$2(E_0-E_p)$ (V)	ET rate constant (cm s^{-1})
0.00	-0.2755	-0.3267	0.1025	0.004509
0.22	-0.2692	-0.3187	0.0991	0.004606
0.44	-0.2621	-0.3114	0.0987	0.004651
0.66	-0.2612	-0.3058	0.0892	0.004786
0.88	-0.2524	-0.2975	0.0901	0.004792
1.10	-0.2443	-0.2881	0.0876	0.004834
1.32	-0.2360	-0.2781	0.0842	0.004890

With the rate constants obtained under different magnetic fields, a best fit to the experimentally obtained $\ln(k_m/k_0)$ vs. magnetic field (H [T]) gives the following equation (Figure 6b):

$$\left(\frac{k_m}{k_0}\right)_{ORR} = \exp(53.99 \cdot H + 0.01) \qquad \textbf{Eq. 6}$$

where k_m and k_0 is the electron transfer rate constant of oxygen reduction with and without magnetic fields, respectively. A similar Co^{III}/Co^{II} redox reaction was observed at the Co_3O_4/ECNFs electrode in the presence of oxygen (no redox peaks in the absence of oxygen), suggesting a coupling of the Co^{III}/Co^{II} redox reaction and the ORR process. The magnetic field effect on the electron transfer kinetics of the Co_3O_4 electrode system focusing on the Co^{III}/Co^{II} redox couple (a reduction peak at around 0.5 V vs. Ag/AgCl) at ECNFs was further analyzed by using the Laviron method derived for a diffusionless electrochemical redox reaction system, because the Co^{III}/Co^{II} redox reaction occurs in the deposited Co_3O_4 film. The standard rate constants (k0) of Co^{III}/Co^{II} were obtained by the fitting of cyclic voltammetry data (Figure 7a) with the function of overpotential vs. m^{-1}, as expressed by Equation (7):

$$A_c = mn^{-\gamma}\left\{1 - m(1+\eta)\exp[f(n)]\int_{\infty}^{\eta} x^{-(1+\gamma)}\exp[-f(x)]dx\right\} \qquad \textbf{Eq. 7}$$

where A_c is the function for the cathodic curve, γ is the fitting coefficient, η=exp[(nF/RT)(Ep-$E0$)], and m=(RT/F)(k^0/nv). In the absence of an external magnetic field, the standard heterogeneous rate constant for the Co_3O_4/ECNFs electrode system is calculated to be about 0.049 s^{-1}. In the presence of an external magnetic field, the standard rate constants are found to

be about 0.063, 0.071, 0.079, 0.086, 0.095, and 0.102 s^{-1} under magnetic fields of 0.22, 0.44, 0.66, 0.88, 1.10, and 1.32 mT (Table 4), respectively.

Table 4.

Magnetic Field (mT)	k_{Co}^{0} (s^{-1})
0.00	0.049±0.011
0.22	0.063±0.005
0.44	0.071±0.008
0.66	0.079±0.004
0.88	0.086±0.007
1.10	0.095±0.003
1.32	0.102±0.004

According to transition state theory, magnetic field-induced degeneracy on unpaired electron spins generates enhanced electron energy states that contribute to the activation energy for electron-transfer reactions. Figure 7b shows schematically the electronic configurations resulting from electron transfer [Co3+ $(e_g^0 t_{2g}^6$ or $e_g^2 t_{2g}^4)$ to Co2+ $(e_g^1 t_{2g}^6$ or $e_g^2 t_{2g}^5)$]. The increase in Zeeman energy, $g\beta HS_p$, in $Co^{3+/2+}$ in the presence of a magnetic field contributes to the activation energy by reducing the net enthalpy of the activation barrier and thereby facilitating the redox reaction rate. The electron transfer rate constant ratio at the electrode surface can be expressed in Arrhenius form described in Equation (8):

$$\frac{k_m}{k_0} = exp\left(\frac{gS_p\beta}{k_B T} \cdot H + \frac{\Delta S_m}{k_B}\right) \quad \textbf{Eq. 8}$$

where g is the magnetic response to an applied magnetic field, S_p is electron spin, β is the Bohr magneton, k_B is Boltzmann's constant, and ΔS_m is the magnetically dependent entropy term. Qualitatively, according to Equation (8), the initial energy is shifted by the Zeeman energy under sufficient magnetic field. Quantitatively, a best fit to the experimentally obtained $\ln(k_m/k_0)$ versus H gives the following equation (Figure 7c):

$$\left(\frac{k_m}{k_0}\right)_{Co} = \exp(437.36 \cdot H + 0.17) \quad \textbf{Eq. 9}$$

According to Equations (6) and (9), in an embodiment, the pre-factor (437.36) of MEET for the Co^{III}/Co^{II} redox reaction in the Co_3O_4-electrode system is much larger than that (53.99) for the ORR at the electrode surfaces. To this end, a general summary statement of the data analysis and discussion can be reached for the above-discussed embodiments: 1) the magnetic field polarization on unpaired electron spin of Co_3O_4 and the energy degeneracy can enhance the kinetics of the Co^{III}/Co^{II} redox reaction (Co^{2+} and Co^{3+} by a CoOOH surface layer) in the Co_3O_4/ECNFs catalytic centers (Figure 7d); and 2) coupling of the Co^{III}/Co^{II} redox reaction and the ORR process facilitate a faster rate of oxygen reduction by the Co_3O_4/ECNFs to fulfill a nearly 4-electron pathway during the oxygen reduction reaction process:

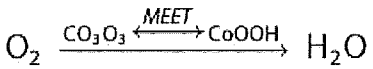

Eq. 10

V. MnO_2 Growth Characterization and Mechanism

Methods for MnO_2 electrodeposition onto the well-aligned ECNFs is described herein, where MnO_2 electrodeposition onto the ECNFs forms a uniform, dense film of MnO_2 having a self-limiting thickness. The alignment of the ECNFs reduces the disordered electron flow, leading to a more uniform electrodeposition process by introducing reaction sites for nucleation of MnO_2 crystallites. Methods for preparing well-aligned ECNFs are described below in EXAMPLE 1.

In this embodiment, a uniform layer of the transition metal oxide, MnO_2, can be electrodeposited on each of the plurality of ECNFs. The transition metal oxide can include MnO_2 that is electrodeposited on each of the plurality of ECNFs, although any other metal oxide or transition metal oxide not inconsistent with the goals of this disclosure can also be electrodeposited, separately or in conjunction with the MnO_2. As described below, Fe_2O_3 can be co-deposited with MnO_2 on ECNFs. In some embodiments, low current electrodeposition techniques are used to grow a fine and firm layer of the metal oxide (e.g., MnO_2). The aforementioned fabrication processes (i.e., electrospinning and electrodeposition) are facial and scalable.

In some instances, a constant low current (e.g. 45 μA) was applied for the electrodeposition by an electrochemical workstation for various times ranging from 2 h to 4 h

under an N_2 atmosphere with an aqueous precursor solution containing 10 mM MnO_2 and 100 mm Na_2SO_4. The composites' structures and morphologies were characterized by scanning electron microscopy (SEM), where Figures 13c and 13d show MnO_2/ECNFs at 2μm and 200nm, respectively, after 2h of electrodeposition and Figures 13e and 13f show MnO_2/ECNFs at 2μm and 200nm, respectively, after 4h of electrodeposition. When the electrodeposition starts, thin films form on the functionalized sites distributed on the fibers (Figures 13c and 13d). As electrodeposition continues, the films begin to grow denser/thicker and the fibers are fully covered (Figures 13e and 13d).

After electrodeposition of 2 h, small balls around the ECNFs present as "kebab"-like structures. Although the SEM images clearly show surface structures corresponding to these firmly merged balls (Fig. 13c and 13d), the ECNFs fibers are not fully covered. After electrodeposition for 4 h, the ECNFs with nanofiber diameter of about 206 nm are decorated by a MnO_2 film with a thickness of about 1710 nm, making a total diameter of about 1916 nm (Fig. 13e and 13f). These data corroborate the inference that the ECNFs' alignment promotes the homogenous electron flow and facilitates uniform MnO_2 growth.

The composites by 4 h electrodeposition were further analyzed by different kinds of techniques. EDX spectrum (Fig. 14a) shows the surface composition is composed of the elements O and Mn. The atomic ratio of O and Mn is close to 2:1, which implies the formation of MnO_2. TGA of ECNFs and MnO_2/ECNFs to 700°C in air was shown in Fig. 14b. Due to the residue solvent evaporation, the ECNFs sample shows a weight loss before 425.0°C. And then the ECNFs sample decomposes until 595.5°C. Unlike ECNFs, the MnO_2/ ECNFs still achieve about 52.8% after 595.5°C, indicating the weight fraction of MnO_2 on the MnO_2/ECNFs sample is about 52.8%. The success of MnO_2 deposition was further confirmed with Raman spectra and FTIR spectra. At Raman shift of 1325 cm^{-1} and 1569 cm^{-1}, the ECNFs sample shows D-band and G-band, respectively. While, for the $_{MnO2}$/ECNFs sample, Mn-O presents at the Raman shift of 624 cm^{-1} (Fig. 14c). Correspondingly, ν(Mn-O) presents at the wavenumber of 643 cm^{-1} and 727 cm^{-1} according to the FTIR spectra (Fig. 3d). And IR transitions at 1176, 1647, and 3263 cm^{-1} are assigned to ν(C-O), ν(C=O), and ν(O-H), respectively. The chemical composition of the MnO_2/ECNFs sample was also investigated by the XPS. The high resolution Mn 2p spectra for MnO_2/ECNFs is presented in Fig. 14e. Two strong peaks at 642.2 and 653.8 eV can be clearly seen, corresponding to the Mn $2p^{3/2}$ and Mn $2p^{1/2}$ spin–orbit peaks of MnO_2, respectively.

Furthermore, the crystal structures of the as-prepared MnO_2/ECNFs were also recorded by XRD (Fig. 14f), the patterns of which can be fully indexed to α-MnO_2 (JCPDS No. 44-0141).

Herein, the excellent electrodeposition of MnO_2 originates from the stable structure of ECNFs, which contributes to a uniform Mn^{2+} flux. The electrochemical reaction occurs according to:

$$Mn^{2+} + 2H_2O \rightarrow MnO_2 + 4H^+ + 2e^- \quad \textbf{Eq. 11}$$

It is known that MnO_2 has different main structural motifs due to edge- or corner-sharing MnO_6 octahedra in different connectivity schemes, resulting in different tunnels extending in a direction parallel to the unit cell. Here, the cations (Na+) were introduced during the synthesis process, but the 1x1 tunnels (with a size of 0.189 nm) are generally too small for Na+ to stabilize the structure, consequently resulting in the formation of α-MnO_2 due to structurally constructed from the double chains of edge- sharing MnO_6 octahedra which are linked at the corners to form 2x2 (with a size of 0.460 nm) and 1x1 tunnel structures. The crystal structure was confirmed by the XRD analysis of MnO_2/ ECNFs by electrodeposition for 2h and 4h. Meanwhile, these cations inside 2x2 tunnels of α-MnO_2 increase the electronic conductivity of the MnO_2/ECNFs system, which indirectly enhance the electrodeposition of α-MnO_2.

VI. Catalytic Properties of MnO_2/ECNFs

The ORR activity was firstly conducted by studying the cyclic voltammetric responses of a bare GC electrode (Fig. 15a). The cathodic peak results from the electrochemical reduction of oxygen and the magnitude of the cathodic peaks increases with increasing of the voltage scan rates. In addition, the peak current, i_p (A), is measured as a function of the square root of the voltage scan rate (v (V/s)), which is found to exhibit a linear dependence (Fig. 15b). The dependence of the peak current position on the square root of the voltage scan rate for the bare GC electrode without modification can be firstly used to characterize the concentration of oxygen in the bulk solution (C, mol/mL) through Randles-Sevcik equation (Note that the slope is obtained from the dependence of i_p (A) on v (V/s)):

$$|slope| = \left(2.99 \times 10^5\right) n^{3/2} \alpha^{1/2} A C D_0^{1/2} \quad \textbf{Eq. 12}$$

where n is the number of electrons exchanged during the electrochemical process, α is the transfer coefficient (reported value of 0.26), A is the active surface area of the bare GC electrode (0.071 cm^2), D_0 is the diffusion coefficient (reported value of $1.95x10^{-5}cm^2/s$). Since the reduction of oxygen to hydrogen peroxide is known at the bare GC electrode, the number of electrons exchanged is 2. When the above constants are applied for absolute value of the slope obtained from Fig. 15b, the oxygen concentration of $3.11x10^{-7}$ mol/mL is extracted.

The cyclic voltammetric responses of the ECNFs modified electrode and MnO_2/ECNFs (2 h and 4 h) modified electrode were examined by varying the scan rates from 20 mV/s to 200 mV/s, which also show an increase in the cathodic peak current with respect to the scan rate as shown in Figs. 16a and 16b. In comparison, there is a marked enhancement in the ORR of the electrode modified with MnO_2/ECNFs (4 h). Note that the anodic peak presented at 0.32 V is attributed to the oxidation reactions between the Mn(IV)/Mn(III) complexes. As mentioned above, Eq. (12) is also used to calculate the number of electrons in the overall electrochemical processes for electrodes modified with super-aligned ECNFs and MnO_2/ECNFs. The peak currents are directly proportional to the square roots of scan rates for both modified electrodes with a slope of $-8.01x10^{-5}$ (ECNFs modified electrode) and $11.59x10^{-4}$ (MnO_2/ECNFs (4 h) modified electrode), respectively (Fig. 16c). Moreover, the slope of a plot of $\log(i_p)$ (i_p is in unit of A) versus potential (potential is in unit of V) (Fig. 16d) and the following equation is used to determine the transfer coefficient:

$$Slope = \frac{-\alpha F}{2.3RT} \quad \textbf{Eq. 13}$$

where R is the gas constant, F is the Faraday's constant, and T is the temperature. The transfer coefficient is obtained to be 0.65 (ECNFs modified electrode) and 0.52 ($_{MnO2}$/ECNFs (4 h) modified electrode), respectively. By using Eq. (12), this value can then be coupled with the active surface area, the diffusion coefficient of oxygen, and the concentration of oxygen to extract the number of electrons exchanged as 2.26 (ECNFs modified electrode) and 3.84 (MnO_2/ECNFs (4 h) modified electrode), respectively. Meanwhile, in comparison, with a transfer coefficient of 0.58 (Fig. 16d) and a slope of $-1.39x10^{-4}$ (Fig. 5c), the number of electrons

exchanged is obtained to be 3.37 for the MnO_2/ECNFs (2 h) modified electrode, because the oxygen and hydrogen peroxide are not effectively confined within the imperfectly fiber-covered MnO_2/ECNFs-GC system. As expected, the voltammetric curve of an ECNFs modified electrode exceeds a 2-electron transfer ORR through an energetically favored association to assist the adsorption and reduction of oxygen molecules, which is characteristics of the activity of ECNFs. However, for the MnO_2/ECNFs modified electrode, considering that the hydrogen peroxide molecule generated from the electrochemical reduction of oxygen to be decomposed repeatedly at the surface of a uniform MnO_2 film, a nearly 4- electron pathway contributed with cycles of oxygen decomposition/regeneration.

Since the catalytic decomposition of hydrogen peroxide typically follows first order kinetics, hydrogen peroxide decomposition at the surface of a uniform MnO_2 film (4 h) was investigated, were a cyclic voltammogram of a MnO_2/ECNFs modified electrode was studied in an N_2 saturated 20 mM KCl electrolyte solution with 1 mM hydrogen peroxide at different scan rates (Fig. 17a). No measureable reduction peak shows for an ECNFs modified electrode in an N_2 saturated 20 mM KCl electrolyte solution with 1 mM hydrogen peroxide. However, a marked increase in the voltammetric performance of the MnO_2/ ECNFs modified electrode was observed as a result from the electrochemical decomposition of hydrogen peroxide successfully taking place at the electrode surface. Furthermore, in the same way, slope of the plot of log(*ip*) versus potential (Fig. 17b inserted subgraph) and Eq. (13) were used to determine the transfer coefficient of 0.09. When the constants of active surface area (0.071 cm^2), diffusion coefficient of hydrogen peroxide (reported value of $1.0x10^{-5}cm^2/s$) and concentration of hydrogen peroxide ($1.0x10^{-6}$ mol/mL) are applied for the slope obtained from the MnO_2/ECNFs modified electrode (Fig. 17b), a n value of 1.91 is extracted. This highly supports that the hydrogen peroxide molecules generated from the electrochemical reduction of oxygen are decomposed by the uniform MnO_2 film. The hydrogen peroxide decomposition by the uniform α-MnO_2 film can likely be ascribed to at least two reasons: one is the open crystal structure of α-MnO_2 with 2x2 tunnels providing favorable surface coordination, such as the higher Miller index (211) and (112) surfaces expressed in the XRD results; and the other is the low oxygen vacancy formation energy providing a favorable thermodynamic pathway for catalytic processes, such as 1.09 eV for (211) and 0.07 eV for (112).

To compare the rate of the hydrogen peroxide generation by ECNFs modified electrodes (O_2-ECNFs) with the hydrogen peroxide decomposition by MnO_2/ECNFs modified electrode (H_2O_2-MnO_2), the electron transfer kinetics should be taken into account. The Gileadi method based upon the determination of critical scan rate (v_c) was further used to evaluate the heterogeneous electron transfer rate constant (k^0). When the experimental results from O_2-ECNFs and H_2O_2-MnO_2 are applied for this analysis, the critical scan rate can be found from the intersection of two lines as Fig. 18 shows. Then the following equation was used to calculate the k^0 (cm/s):

$$\log\left(k^0\right) = -0.48\alpha + 0.52 + \log\left[\frac{nF\alpha v_c D_0}{2.303RT}\right]^{1/2} \quad \textbf{Eq. 14}$$

By using this method, associated with the transfer coefficient, number of electron transfer, and diffusion coefficient obtained above, the value of heterogeneous electron transfer rate constant for O_2-ECNFs and H_2O_2-MnO_2 is calculated to be 1.30×10^{-2} cm/s and 1.37×10^{-2} cm/s, respectively. The rate of hydrogen peroxide decomposition by MnO_2/ECNFs modified electrode is faster than the electrochemical generation process by ECNFs modified electrodes, which may be partly ascribed to the presence of K+ inside the 2x2 tunnels of the α-MnO_2 enhancing the electrocatalytical performance of the catalyst.

VII. 4-electron pathway mechanism for MnO_2/ECNFs

A 4-electron pathway mechanism is shown in Fig. 19 based on the catalytic activity analysis in Section V above. When the oxygen molecule has been adsorbed onto the MnO_2/ECNF-GC electrode surfaces, the redox between MnO_2 species assists the charge transfer involved in oxygen reduction, and the first step undergos a 2-electron pathway forming hydrogen peroxide (Eq. (15):

$$O_{2\,ads} + 2H^+ + 2e^- \rightarrow H_2O_2 \quad \textbf{Eq. 15}$$

The electrochemically generated hydrogen peroxide can then be decomposed to water via a disproportionation reaction before it escapes into the bulk solution by a uniform α-MnO_2 film (Eq. (16)), though an electrochemical decomposition to OH^- may occur:

$$2H_2O_2 \xrightarrow{\alpha\text{-}MnO_2} O_2 + 2H_2O \qquad \textbf{Eq. 16}$$

The rate of hydrogen peroxide decomposition by α-MnO_2/ ECNFs modified electrode is faster than the electrochemical generation process by ECNFs modified electrode, and the presence of K+ inside the 2x2 channels of the α-MnO_2 has a strong beneficial effect on the electrochemical performance of the catalyst, which improves the efficiency of the ORR process shown above in the results. A half of the oxygen concentration shown in Eq. (16) is electrochemically regenerated after each cycle, which reduces the risk of the fuel cell degradation for practical uses. As a result, Eq. (15) and Eq. (16) occurring in series give the α-MnO_2/ECNF-GC catalytic system as much efficiency as a 4-electron pathway:

$$O_2 + 4H^+ + 4e^- \rightarrow 2H_2O \qquad \textbf{Eq. 17}$$

Considering that a cycle of decomposition/regeneration of a half of the oxygen concentration at the MnO_2/ECNF-GC electrode, the contribution for the electron pathway from the bifunctional catalyst can be divided into two parts, i.e. the first 2-electron transfer oxygen reduction to hydrogen peroxide at the GC-MnO_2 interfaces, and following hydrogen peroxide decomposition at the α-MnO_2 surfaces. Fig. 19 shows the proposed reactions where *i* is the number of cycles regarding the reduction of oxygen and regeneration of oxygen with respect to the oxygen and hydrogen peroxide confinement ability. The total number electron pathway can be expressed:

$$N = 2\sum_{i=0}^{\infty}\left(\frac{1}{2}\right)_{GC-MnO_2} + 2\sum_{i=0}^{\infty}\left(\frac{1}{2}\right)_{MnO_2} \qquad \textbf{Eq. 18}$$

where *N* is the number-electron pathway, sigma notation is the contribution from different parts, and *i* is the number of cycles regarding the reduction of oxygen and regeneration of oxygen with respect to the oxygen and hydrogen peroxide confinement ability in the aligned MnO_2/ECNFs structures. As the result analysis provided above, the number of electrons exchanged is obtained to be 3.37 (*i* is estimated to be 3) for the 2-hour electrodeposited MnO_2/ECNF electrode (MnO_2 ununiformly covered at ECNFs), because the oxygen and hydrogen peroxide are not completely reduced within the MnO_2/ECNFs-GC system due to the insufficient catalytic activity and

confinement (number of cycling). Whereas at 4-hour deposited MnO_2/ECNFs, the number of electrons exchanged is achieved to be at least 3.84, suggesting a large cycle number (namely good confinement, *i* is estimated to be 5) and excellent catalytic activity are obtained from the uniform electrodeposition of α-MnO_2 on ECNFs.

OER activity was also investigated for MnO_2 coated ECNFs. Fig. 21a illustrates OER current densities for MnO_2 coated ECNFs fabricated according to methods described herein. Magnetic fields of varying strength were applied during the OER reaction. Fig. 21b illustrates OER current densities for MnO_2 coated ECNFs in the absence of magnetic field application. Presence of the magnetic field produced slightly higher current densities for OER.

In summary, the methods described herein demonstrate a new strategy for uniformly electrodepositing an α-MnO_2 film on aligned ECNFs. In contrast to earlier studies with an inhomogeneous surface coverage, the reported α-MnO_2 film with a 4 h–45 mA electrodeposition was uniform with a thickness of 1710 nm. From the electrocatalytic performance studies, the bifunctional catalyst system of α-MnO_2/ECNFs-GC displayed a 3.84-electron pathway through the rapid decomposition of hydrogen peroxide at the α-MnO_2 surfaces. The analysis of electron transfer kinetics suggested a faster hydrogen peroxide decomposition than its generation from reduction of oxygen, and a two-step four-electron pathway cycling mechanism was proposed to give an insightful understanding of the electrocatalytic ORR at the bifunctional catalyst system. These findings represent significant improvement in stable metal oxide/carbonaceous nano-material-based oxygen reduction catalysts.

EXAMPLE 1

Fabrication of super-aligned ECNFs

A 10 wt% polyacrylonitrile (PAN; M_w=150000) solution in dimethylformamide was electrospun onto the collector. The applied positive voltage was 18 kV and the distance between the needle tip and the collector was 15 cm. The collector maintained a rate of 2000 rpm during the electrospinning process to form well-aligned precursors. The obtained sheets were then put into an oxidation and annealing furnace for stabilization to ensure that the fibers did not melt during pyrolysis. The heating rate was 1 °C min^{-1} from room temperature to 280 °C and after which this temperature was maintained for 6 h. The as-stabilized nanofibers were finally

carbonized at 1200°C for 1 h at a heating rate of 5°C min^{-1} under N_2 atmosphere to yield high mechanical strength ECNFs.

EXAMPLE 2

Co_3O_4 electrodeposition on ECNFs

After the well-aligned ECNFs were prepared according to Example 1, Co_3O_4 was electrodeposited onto 1 cm^2 ECNFs with a three-electrode setup with a charging current of 50 mA performed on a bio-logic VMP3 electrochemical workstation. Here, a gold electrode coated with ECNFs, a platinum wire, and Ag/AgCl were used as the working electrode, the counter electrode, and the reference electrode, respectively. To assure that the deposition of Co_3O_4 took place uniformly and firmly at the ECNFs' surfaces, the ECNFs electrode was pretreated with 2% HNO_3 solution at 60°C for 2 h to introduce OH and COOH groups to facilitate the deposition. An aqueous precursor solution containing 20 mm Co_SO_4 and 100 mm Na_2SO_4 was used as the supporting electrolyte. After deposition, the working electrodes were washed with deionized water and the samples were dried.

EXAMPLE 3

MnO_2 Electrodeposition on ECNFs

After the super-aligned ECNFs were prepared according to Example 1, MnO2 was electrodeposited onto 1 cm^2 ECNFs with a three-electrode setup using a charging current of 45 μA performed on a Bio-logic VMP3 electrochemical (EC) workstation (Fig. 20). Here, a gold electrode taped with ECNFs, a platinum wire, and an Ag/AgCl were used as the working electrode (WE), the counter electrode (CE), and the reference electrode (RE), respectively. To assure that the deposition of MnO_2 took place uniformly and firmly at the ECNFs' surfaces, the ECNFs electrode was prior-treated with 4 M HNO_3 solution at 70°C for 2 h to introduce -OH and -COOH groups to facilitate the deposition. An aqueous precursor solution containing 10 mM $MnSO_4$ and 100 mM Na_2SO_4 was used as the supporting electrolyte. After the deposition, the working electrodes were washed with deionized water and then dried at 80°C for 3 h.

EXAMPLE 4

Fe_2O_3 Electrodeposition on ECNFs

After the super-aligned ECNFs were prepared, Fe_2O_3 was electrodeposited onto 1 cm^2 ECNFs with a three-electrode setup using a charging current of 50 μA performed on a bio-logic

VMP3 electrochemical workstation. Here, a gold electrode taped with ECNFs, a platinum wire, and an Ag/AgCl were used as the working electrode, the counter electrode, and the reference electrode (Fisher Scientific), respectively. To assure that the deposition of Fe_2O_3 took place uniformly and firmly at the ECNFs' surfaces, the ECNFs electrode was prior-treated with 4 M HNO_3 (J.T. Baker) solution at 70 °C for 2 h to introduce –OH and –COOH groups to facilitate the deposition. An aqueous precursor solution containing 100 mM $FeSO_4$ (ACROS Organics) was used as the supporting electrolyte. After the deposition, the working electrodes were washed with deionized water and then dried at 80 °C for 5 h.

The Fe_2O_3 coated ECNFs were tested for OER activity. Fig. 22a illustrates OER current densities for the Fe_2O_3 coated ECNFs under application of magnetic fields of varying strength. Fig. 22b illustrates OER current densities for the Fe_2O_3 coated ECNFs in the absence of magnetic field application.

EXAMPLE 5

Fe_2O_3-MnO_2 Electrodeposition on ECNFs

For the Fe_2O_3-MnO_2/ECNFs, all of the steps are the same as Fe_2O_3 electrodeposition in Example 4, except an aqueous precursor solution containing 50 mM $FeSO_4$ and 50 mM $MnSO_4$ (ACROS Organics) was used as the supporting electrolyte. Fig. 23 is a SEM of the Fe_2O_3-MnO_2 coated ECNFs.

The Fe_2O_3-MnO_2 coated ECNFs were tested for OER activity. Fig. 24a illustrates OER current densities for the Fe_2O_3-MnO_2 coated ECNFs under application of magnetic fields of varying strength. Fig. 24b illustrates OER current densities for the Fe_2O_3-MnO_2 coated ECNFs in the absence of magnetic field application. Substantial increases in current densities were observed for the Fe_2O_3-MnO_2 coating ECNFs relative to the MnO_2 coated ECNFs of Figs. 21a and 21b and the Fe_2O_3 coated ECNFs of Figs. 22a and 22b. Fig. 24c is a Tafel plot illustrating increased OER efficiencies of the Fe_2O_3-MnO_2 coated ECNFs with increasing magnetic field strength.

Various embodiments of the invention have been described in fulfillment of the various objectives of the invention. It should be recognized that these embodiments are merely illustrative of the principles of the invention. Numerous modifications and adaptations thereof will be readily apparent to those skilled in the art without departing from the spirit and scope of the invention.

CLAIMS

1. A method of enhancing efficiency of an oxygen evolution reaction (OER), oxygen reduction reaction (ORR), or hydrogen evolution reaction (HER) comprising:

increasing total number electron pathway of the OER, ORR, or HER by coating one or more surfaces of an electrode participating in the OER, ORR, or HER with one or more metal oxides.

2. The method of claim 1, wherein the one or more metal oxides comprise a transition metal oxide.

3. The method of claim 1, wherein metal of the oxide is paramagnetic.

4. The method of claim 2, wherein transition metal of the oxide is paramagnetic.

5. The method of claim 2, wherein transition metal of the oxide is selected from Groups IIIB-VIIIB of the Periodic Table.

6. The method of claim 1, wherein the coating has structure to confine reaction products created at the electrode.

7. The method of claim 6, wherein one or more of the reaction products undergo oxidation or reduction by the electrode.

8. The method of claim 1, wherein the metal oxide comprises one or more dopants.

9. The method of claim 8, wherein dopants are selected from the group consisting of alkali metals, alkaline earth metals and mixtures thereof.

10. The method of claim 1, wherein metal oxide is deposited one or more carbon nanostructures of the electrode.

11. The method of 10, wherein the one or more carbon nanostructures comprise nanofibers, nanotubes, nanospheres, nanosheets, graphene, nanodots or combinations thereof.

12. The method of claim 11, wherein the carbon nanostructures are aligned carbon nanofibers.

13. The method of claim 1, wherein the total number electron pathway of the ORR is at least 3.4.

14. The method of claim 1, wherein the total number electron pathway of the ORR is 3.6 to 4.

15. The method of claim 1, wherein the total number electron pathway of the ORR is 3.85 to 4.

16. The method of claim 1, wherein the total number electron pathway of the ORR is 3.9 to 4.

17. The method of claim 1, wherein the metal oxide comprises manganese oxide or cobalt oxide.

18. The method of claim 1, further comprises applying a magnetic field to the metal oxide coated electrode.

19. The method of claim 18, wherein the applied magnetic field has a magnitude of 0.1 to 1000 mT.

20. A method of enhancing efficiency of an oxygen evolution reaction (OER), oxygen reduction reaction (ORR), or hydrogen evolution reaction (HER) comprising:

increasing total number electron pathway of the OER by conducting the OER, ORR, or HER in an applied magnetic field.

21. The method of claim 20, wherein the applied magnetic field has a magnitude of 0.1 to 1000 mT.

22. The method claim 21, wherein the total number electron pathway of the ORR is at least 3.4.

23. The method of claim 21, wherein the total number electron pathway of the ORR is 3.6 to 4.

24. The method of claim 21, wherein the total number electron pathway of the ORR is 3.85 to 4.

25. The method of claim 20, wherein an electrode participating in the OER, ORR, or HER comprises one or more paramagnetic species.

26. The method of claim 25, wherein the paramagnetic species is a transition metal.

27. The method of claim 26, wherein the transition metal is selected from Groups IIIB-VIIIB of the Periodic Table.

28. The method of claim 21, wherein an electrode participating in the OER, ORR, or HER is coating with one or more metal oxides.

29. The method of claim 28, wherein the one or more metal oxides comprise a transition metal oxide.

30. The method of claim 28, wherein the coating has structure to confine reaction products created at the electrode.

31. The method of claim 30, wherein one or more of the reaction products undergo oxidation or reduction by the electrode.

32. The method of claim 28, wherein the metal oxide comprises one or more dopants.

33. The method of claim 32, wherein dopants are selected from the group consisting of alkali metals, alkaline earth metals and mixtures thereof.

34. An energy generation device comprising:

an electrochemical cell comprising one or more electrodes for performing an oxygen evolution reaction (OER), oxygen reduction reaction (ORR), or hydrogen evolution reaction (HER); and

a magnetic field source for application of a magnetic field to the one or more electrodes during the OER, ORR or HER.

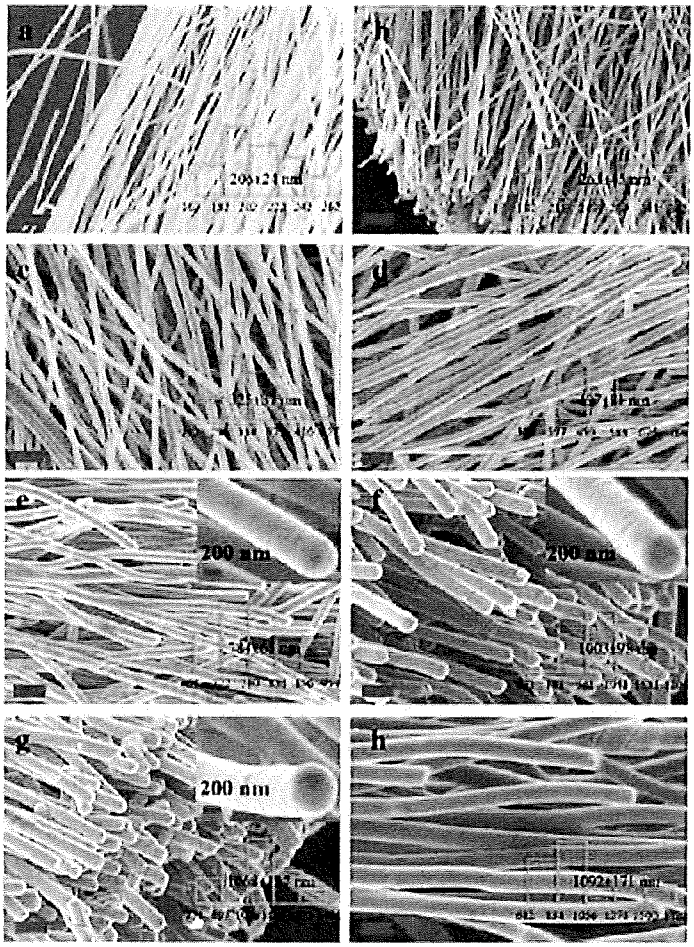

FIG. 1

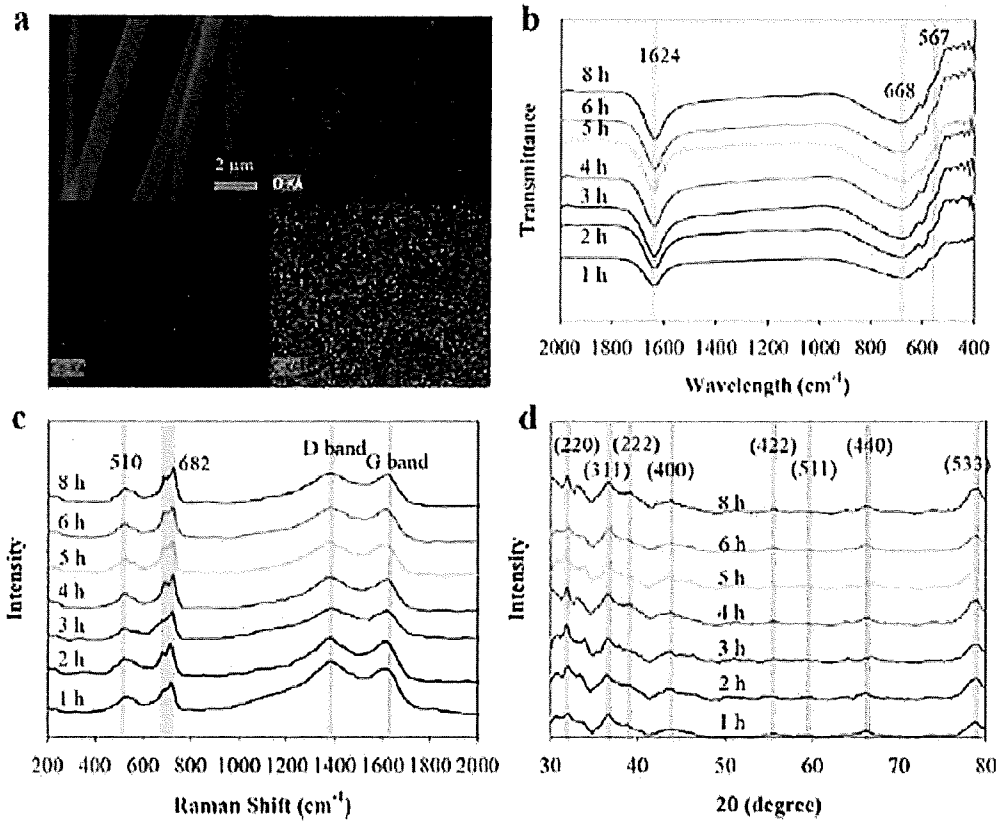
a
2 μm
0 nA
b
1624
567
668
8 h
6 h
5 h
4 h
3 h
2 h
1 h
Transmittance
2000 1800 1600 1400 1200 1000 800 600 400
Wavelength (cm-1)
c
510
682
D band
G band
Intensity
200 400 600 800 1000 1200 1400 1600 1800 2000
Raman Shift (cm-1)
d
(220)
(222)
(311)
(400)
(422)
(511)
(440)
(533)
Intensity
30 40 50 60 70 80
2θ (degree)

FIG. 2

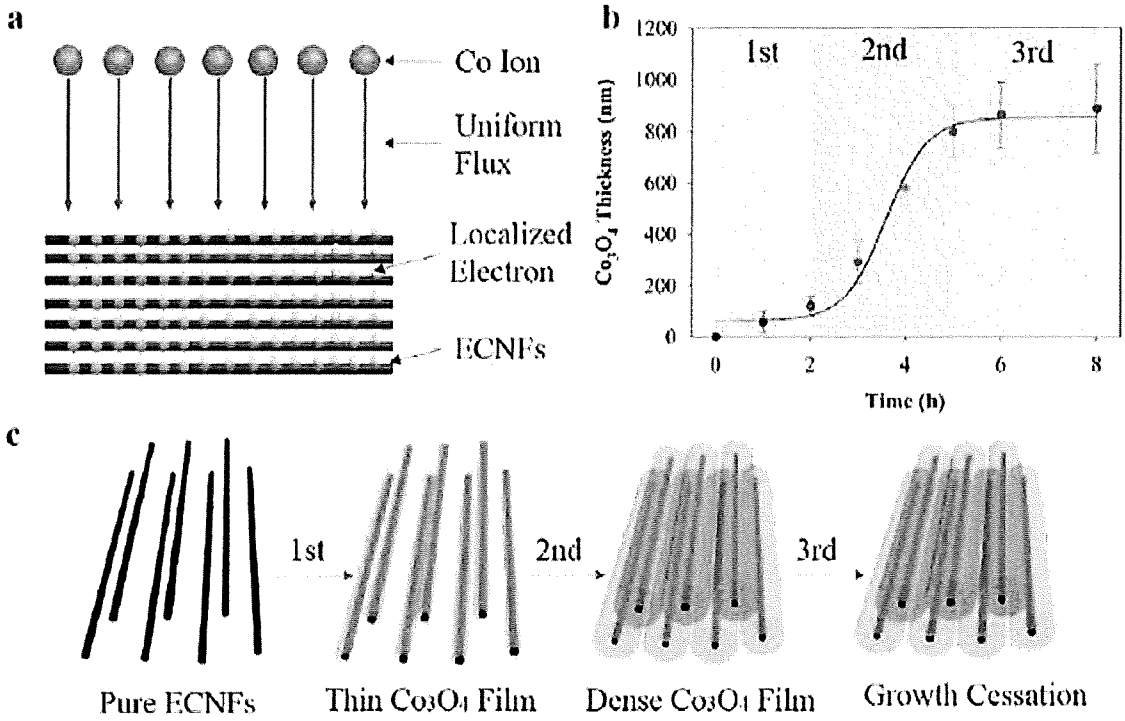
a
Co Ion
Uniform Flux
Localized Electron
ECNFs
b
1st
2nd
3rd
Co_3O_4 Thickness (nm)
1200
1000
800
600
400
200
0
0
2
4
6
8
Time (h)
c
1st
2nd
3rd
Pure ECNFs
Thin Co_3O_4 Film
Dense Co_3O_4 Film
Growth Cessation

FIG. 3

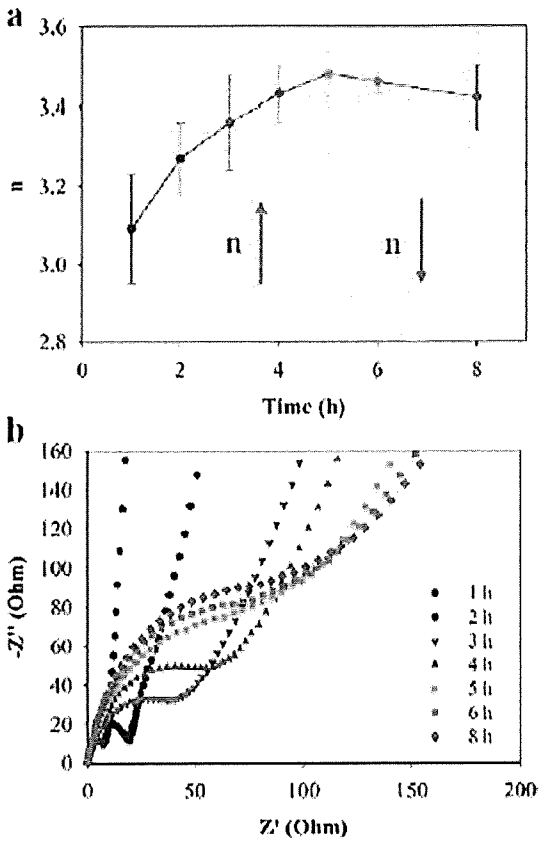
a
3.6
3.4
3.2
3.0
2.8
n
n
n
0
2
4
6
8
Time (h)
b
160
140
120
100
80
60
40
20
0
-Z'' (Ohm)
0
50
100
150
200
Z' (Ohm)
1 h
2 h
3 h
4 h
5 h
6 h
8 h

FIG. 4

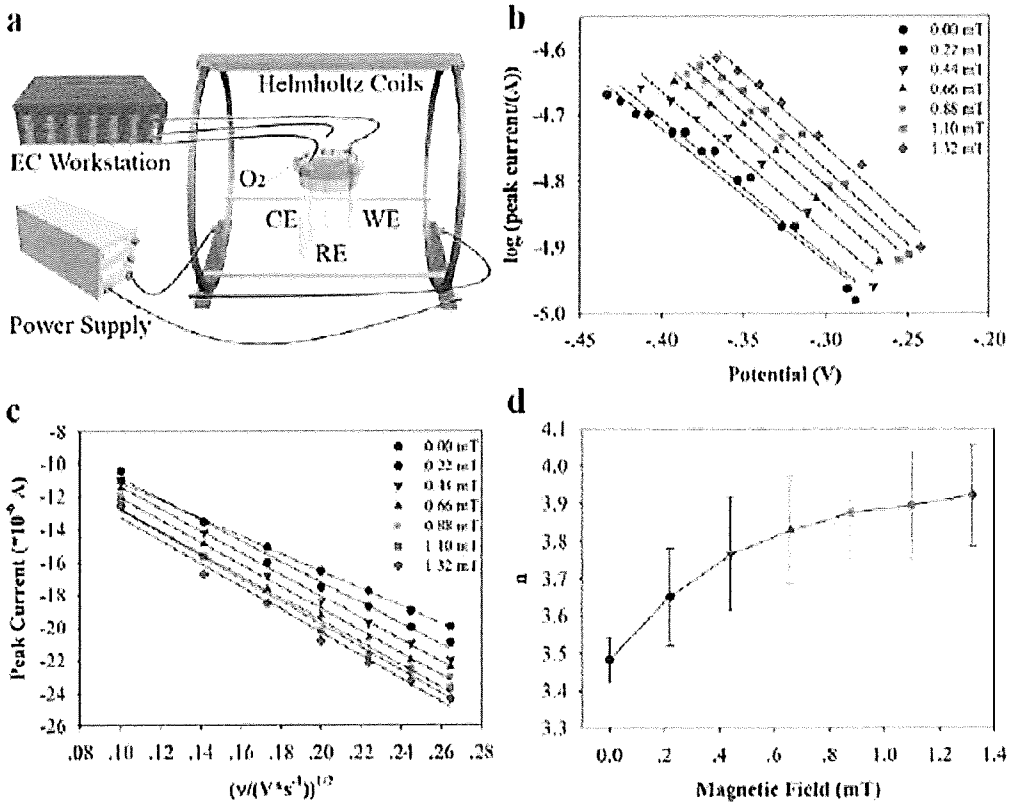
a
Helmholtz Coils
EC Workstation
O2
CE
WE
RE
Power Supply
b
log (peak current/(A))
Potential (V)
c
Peak Current (*10^-6 A)
d
α
Magnetic Field (mT)

FIG. 5

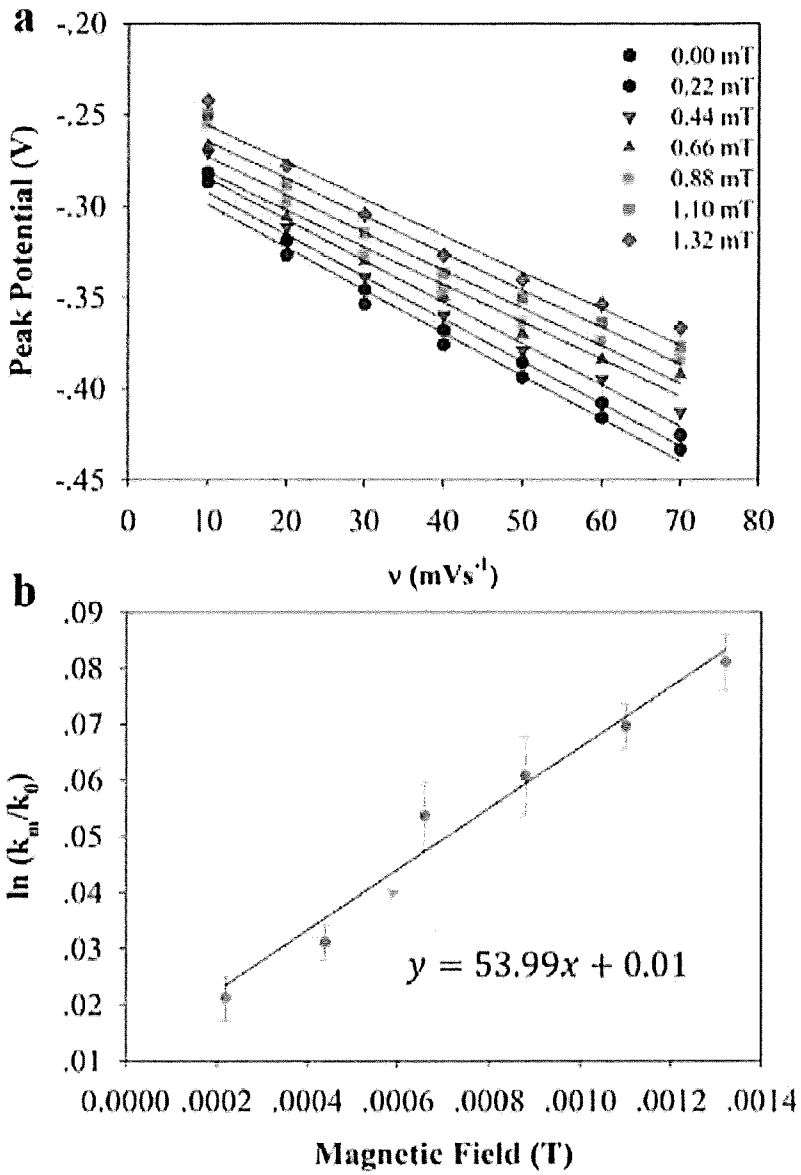
a
-.20
-.25
-.30
-.35
-.40
-.45
Peak Potential (V)
0.00 mT
0.22 mT
0.44 mT
0.66 mT
0.88 mT
1.10 mT
1.32 mT
0
10
20
30
40
50
60
70
80
ν (mVs-1)
b
.09
.08
.07
.06
.05
.04
.03
.02
.01
ln (km/k0)
y = 53.99x + 0.01
0.0000
.0002
.0004
.0006
.0008
.0010
.0012
.0014
Magnetic Field (T)

FIG. 6

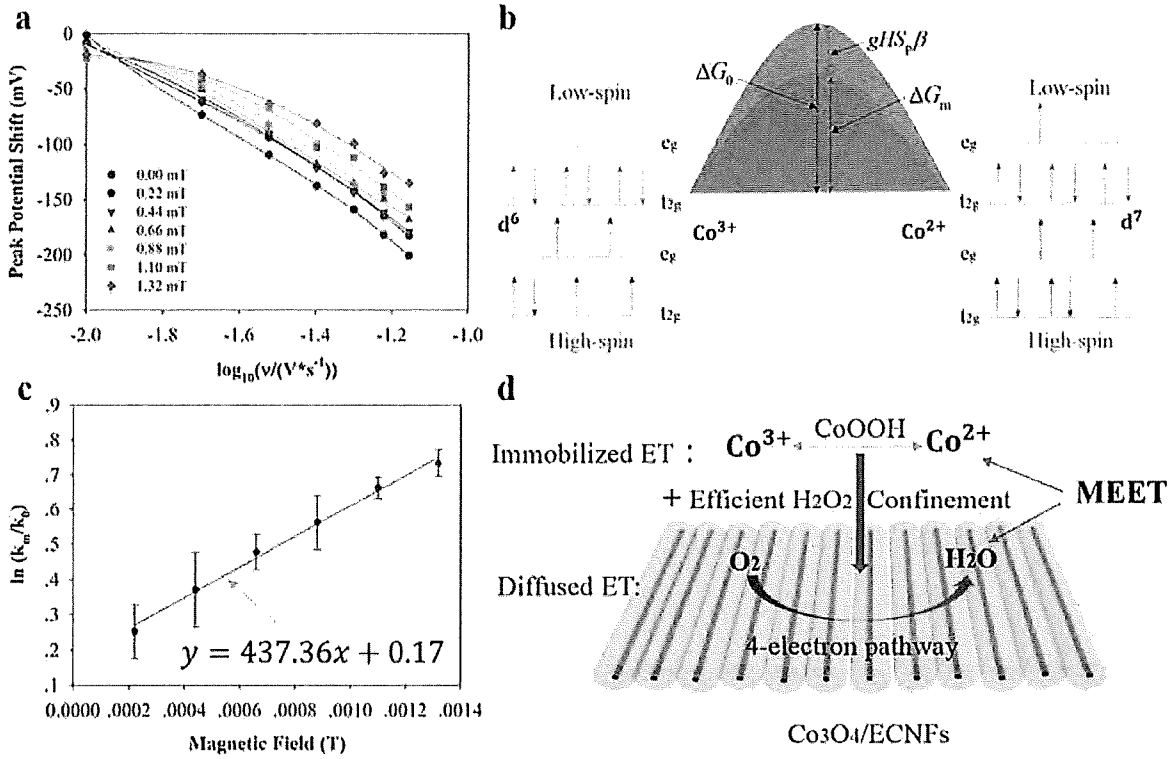
a
Peak Potential Shift (mV)
0
-50
-100
-150
-200
-250
-2.0
-1.8
-1.6
-1.4
-1.2
-1.0
log10(v/(V*s-1))
0.00 mT
0.22 mT
0.44 mT
0.66 mT
0.88 mT
1.10 mT
1.32 mT
b
Low-spin
ΔG0
gHSpβ
ΔGm
Low-spin
eg
t2g
d6
Co3+
Co2+
d7
High-spin
High-spin
c
ln (km/k0)
y = 437.36x + 0.17
0.0000 .0002 .0004 .0006 .0008 .0010 .0012 .0014
Magnetic Field (T)
d
Immobilized ET :
Co3+
CoOOH
Co2+
+ Efficient H2O2 Confinement
MEET
Diffused ET:
O2
H2O
4-electron pathway
Co3O4/ECNFs

FIG. 7

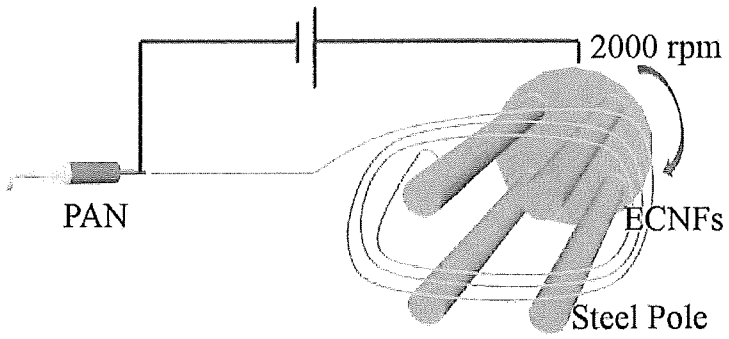
2000 rpm
PAN
ECNFs
Steel Pole

FIG. 8

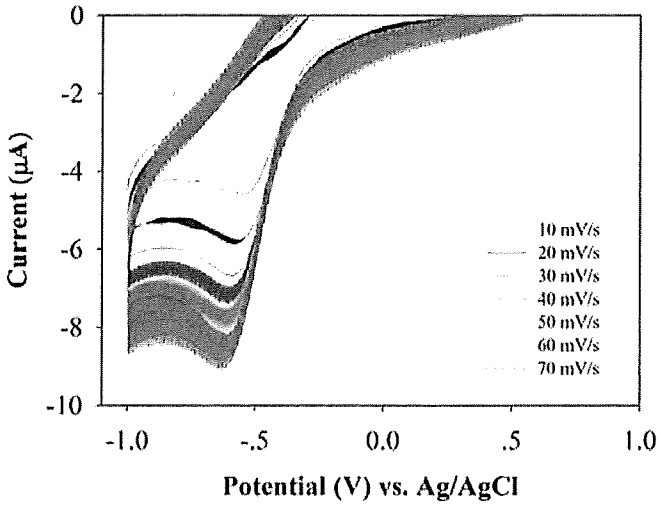
0
-2
-4
-6
-8
-10
Current (μA)
-1.0
-.5
0.0
.5
1.0
Potential (V) vs. Ag/AgCl
10 mV/s
20 mV/s
30 mV/s
40 mV/s
50 mV/s
60 mV/s
70 mV/s

FIG. 9

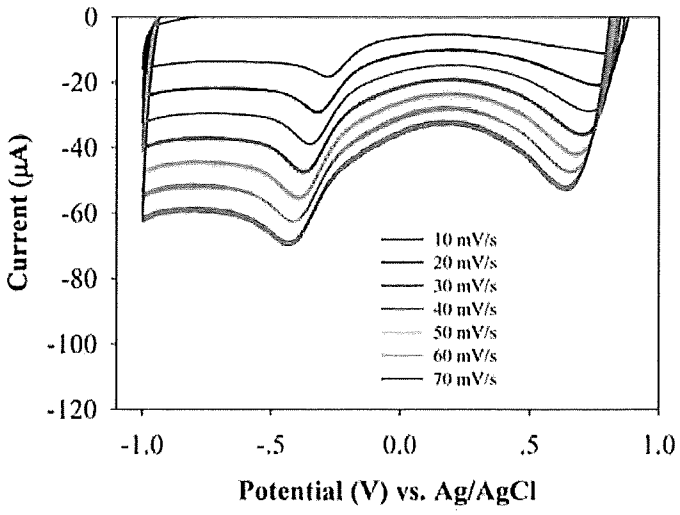
0
-20
-40
-60
-80
-100
-120
Current (μA)
-1.0
-.5
0.0
.5
1.0
Potential (V) vs. Ag/AgCl
10 mV/s
20 mV/s
30 mV/s
40 mV/s
50 mV/s
60 mV/s
70 mV/s

FIG. 10

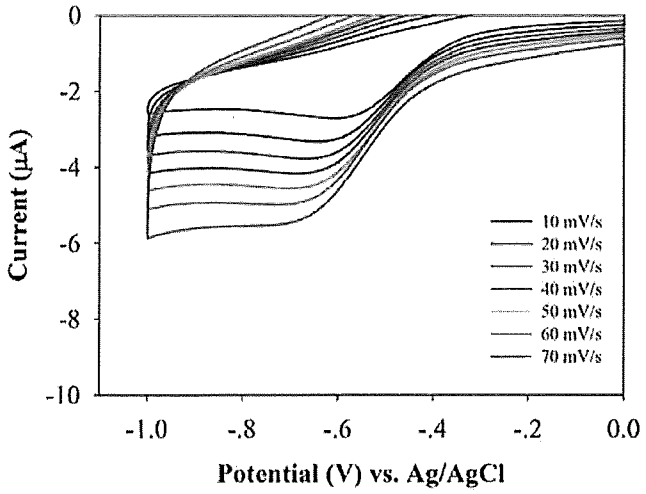
0
-2
-4
-6
-8
-10
Current (μA)
-1.0
-.8
-.6
-.4
-.2
0.0
Potential (V) vs. Ag/AgCl
10 mV/s
20 mV/s
30 mV/s
40 mV/s
50 mV/s
60 mV/s
70 mV/s

FIG. 11

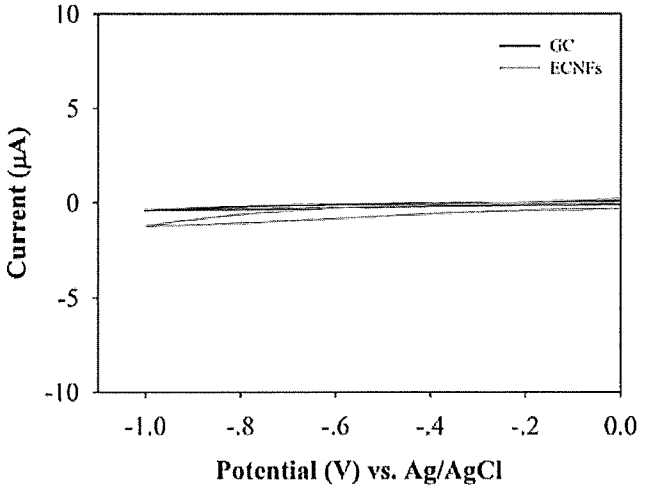
10
5
0
-5
-10
Current (μA)
-1.0
-.8
-.6
-.4
-.2
0.0
Potential (V) vs. Ag/AgCl
GC
ECNFs

FIG. 12

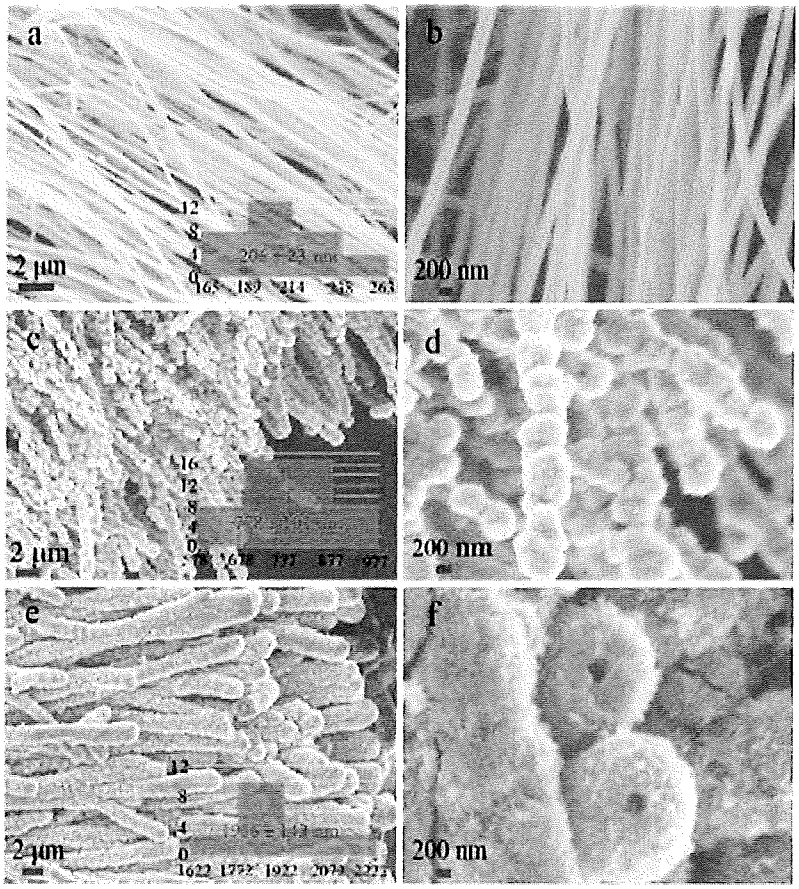

FIG. 13

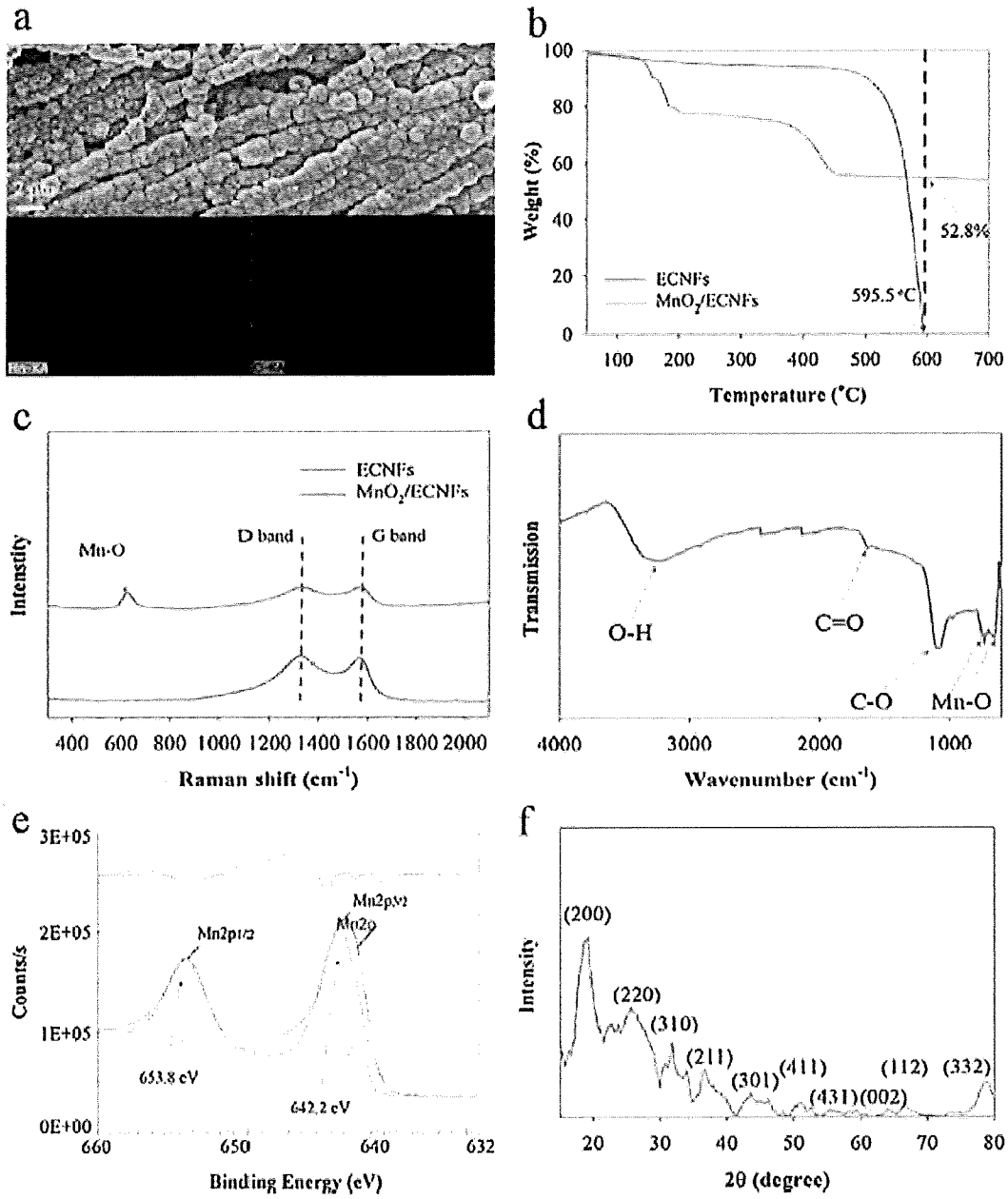
a
b
100
80
60
40
20
0
Weight (%)
52.8%
ECNFs
MnO2/ECNFs
595.5 °C
100 200 300 400 500 600 700
Temperature (°C)
c
ECNFs
MnO2/ECNFs
Mn-O
D band
G band
Intenstity
400 600 800 1000 1200 1400 1600 1800 2000
Raman shift (cm-1)
d
Transmission
O-H
C=O
C-O
Mn-O
4000 3000 2000 1000
Wavenumber (cm-1)
e
3E+05
2E+05
1E+05
0E+00
Counts/s
Mn2p1/2
Mn2p3/2
Mn2p
653.8 eV
642.2 eV
660 650 640 632
Binding Energy (eV)
f
Intensity
(200)
(220)
(310)
(211)
(301)
(411)
(431)
(002)
(112)
(332)
20 30 40 50 60 70 80
2θ (degree)

FIG. 14

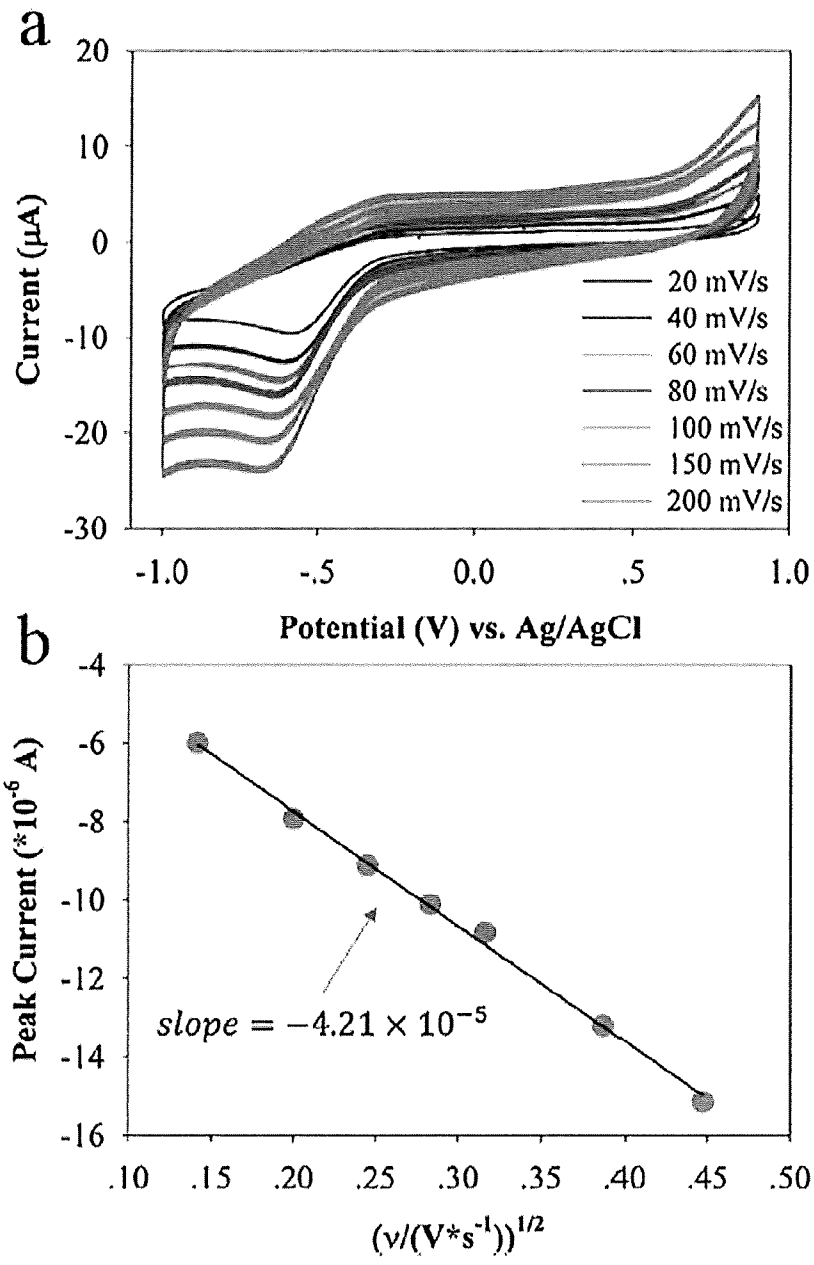
a
20
10
0
-10
-20
-30
Current (μA)
-1.0
-.5
0.0
.5
1.0
Potential (V) vs. Ag/AgCl
20 mV/s
40 mV/s
60 mV/s
80 mV/s
100 mV/s
150 mV/s
200 mV/s
b
-4
-6
-8
-10
-12
-14
-16
Peak Current (*10^-6 A)
slope = −4.21 × 10^−5
.10
.15
.20
.25
.30
.35
.40
.45
.50
(ν/(V*s^-1))^1/2

FIG. 15

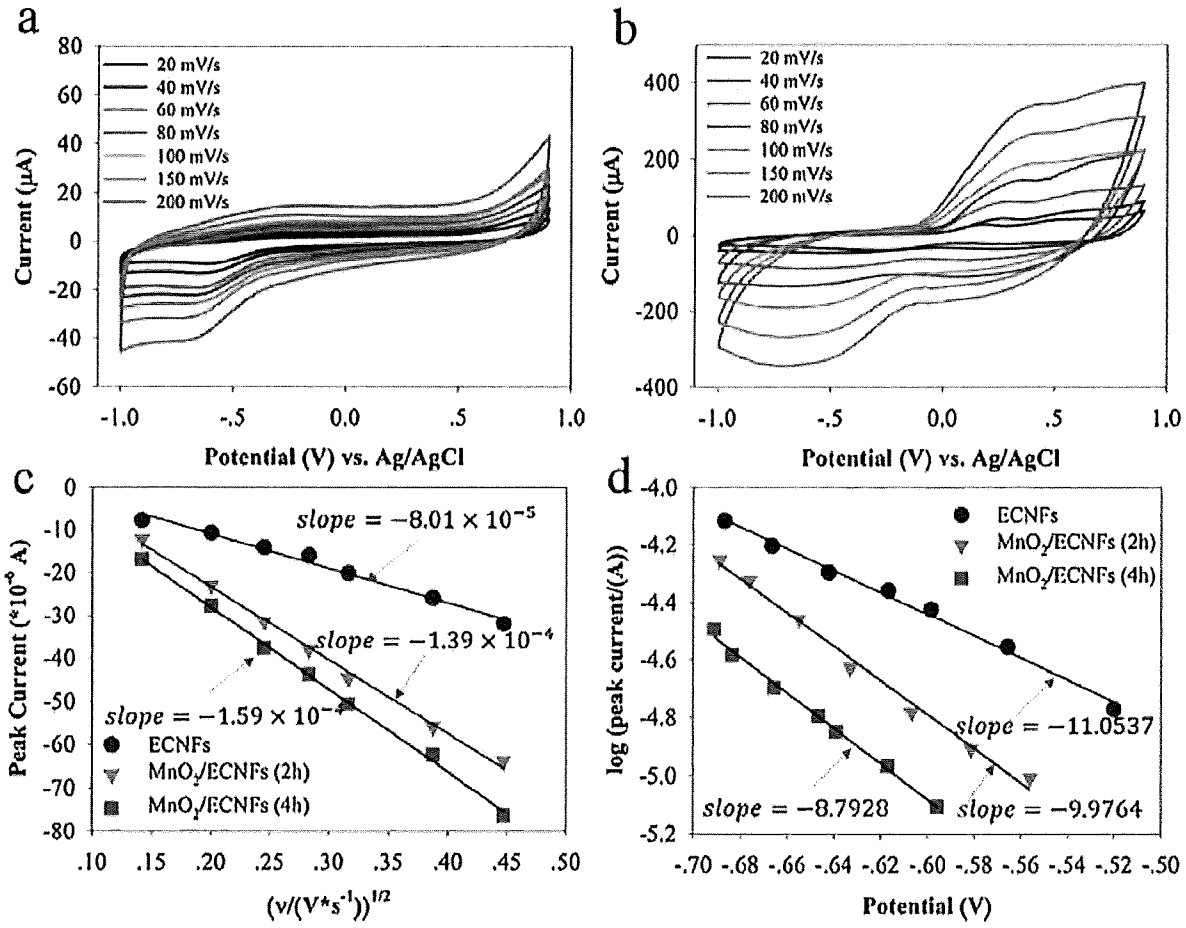
a
20 mV/s
40 mV/s
60 mV/s
80 mV/s
100 mV/s
150 mV/s
200 mV/s
Current (μA)
Potential (V) vs. Ag/AgCl
b
20 mV/s
40 mV/s
60 mV/s
80 mV/s
100 mV/s
150 mV/s
200 mV/s
Current (μA)
Potential (V) vs. Ag/AgCl
c
slope = −8.01 × 10⁻⁵
slope = −1.39 × 10⁻⁴
slope = −1.59 × 10⁻⁴
ECNFs
MnO2/ECNFs (2h)
MnO2/ECNFs (4h)
Peak Current (*10⁻⁶ A)
(v/(V*s⁻¹))^1/2
d
ECNFs
MnO2/ECNFs (2h)
MnO2/ECNFs (4h)
slope = −11.0537
slope = −8.7928
slope = −9.9764
log (peak current/(A))
Potential (V)

FIG. 16

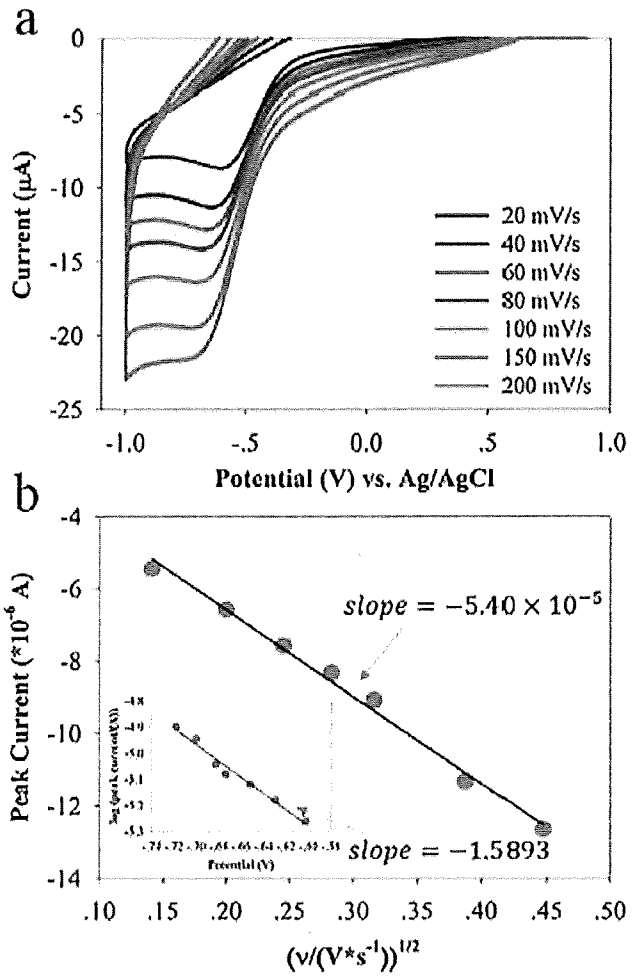
a
Current (μA)
0
-5
-10
-15
-20
-25
-1.0
-.5
0.0
.5
1.0
Potential (V) vs. Ag/AgCl
20 mV/s
40 mV/s
60 mV/s
80 mV/s
100 mV/s
150 mV/s
200 mV/s
b
Peak Current (*10^-6 A)
-4
-6
-8
-10
-12
-14
.10
.15
.20
.25
.30
.35
.40
.45
.50
(ν/(V*s^-1))^1/2
slope = −5.40 × 10^−5
slope = −1.5893

FIG. 17

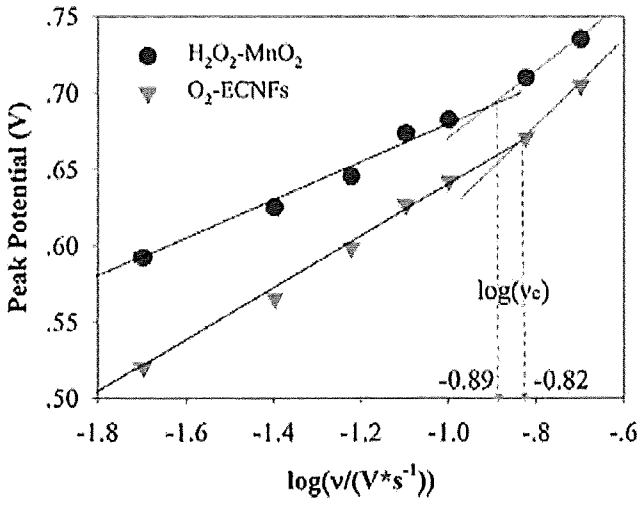
Peak Potential (V)
.75
.70
.65
.60
.55
.50
-1.8
-1.6
-1.4
-1.2
-1.0
-.8
-.6
log(ν/(V*s^-1))
H2O2-MnO2
O2-ECNFs
log(νc)
-0.89
-0.82

FIG. 18

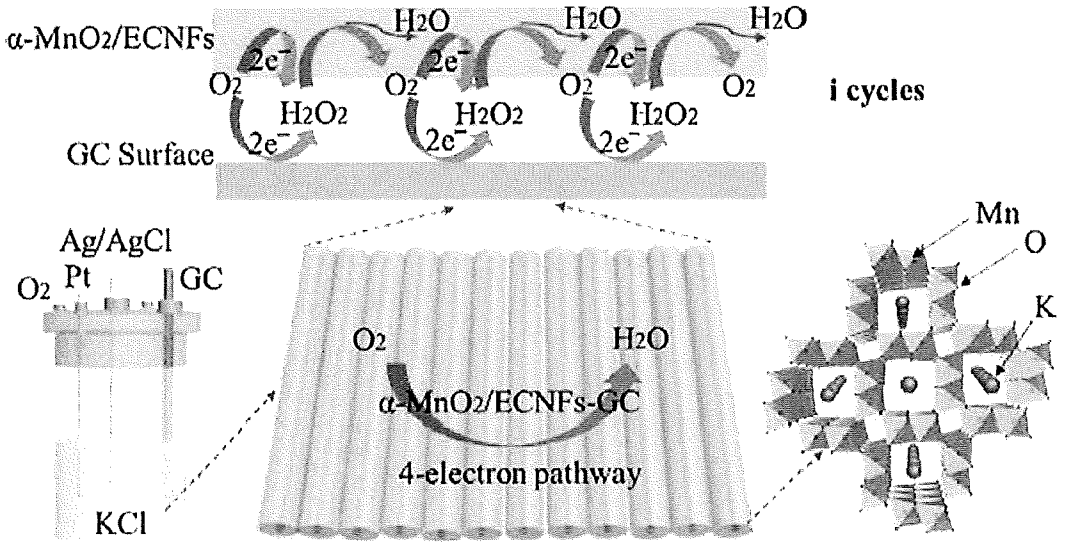
α-MnO2/ECNFs
H2O
H2O
H2O
2e⁻
2e⁻
2e⁻
O2
O2
O2
O2
i cycles
H2O2
H2O2
H2O2
2e⁻
2e⁻
2e⁻
GC Surface
Ag/AgCl
O2 Pt
GC
KCl
O2
H2O
α-MnO2/ECNFs-GC
4-electron pathway
Mn
O
K

FIG. 19

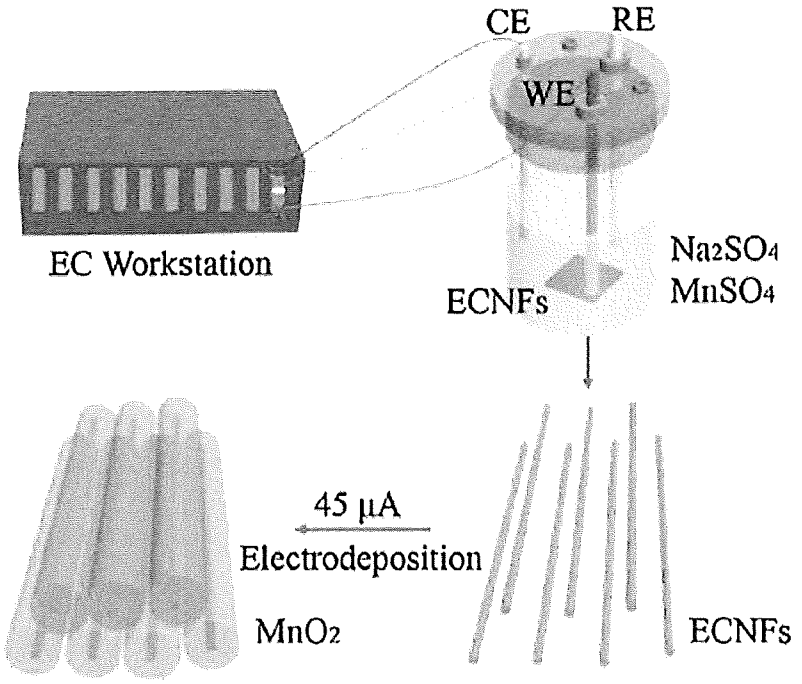
CE
RE
WE
EC Workstation
ECNFs
Na2SO4
MnSO4
45 μA
Electrodeposition
MnO2
ECNFs

FIG. 20

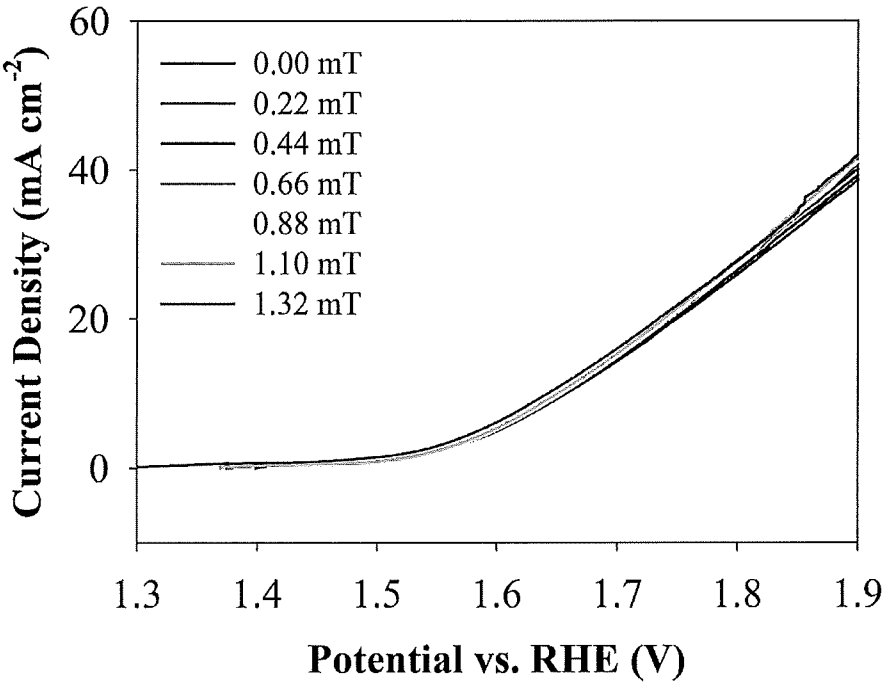
60
40
20
0
Current Density (mA cm-2)
0.00 mT
0.22 mT
0.44 mT
0.66 mT
0.88 mT
1.10 mT
1.32 mT
1.3
1.4
1.5
1.6
1.7
1.8
1.9
Potential vs. RHE (V)

FIG. 21a

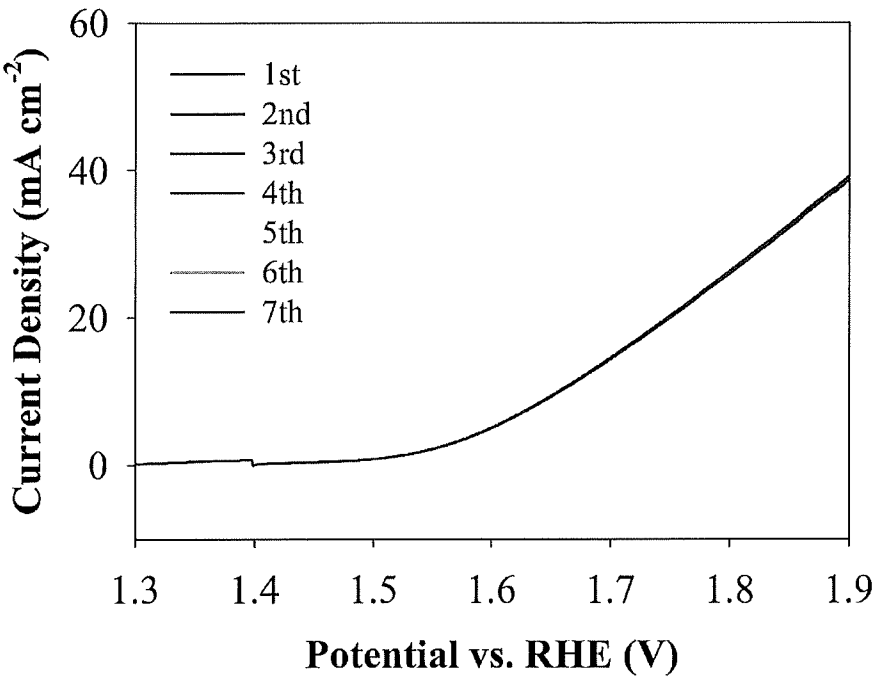
60
40
20
0
Current Density (mA cm-2)
1st
2nd
3rd
4th
5th
6th
7th
1.3
1.4
1.5
1.6
1.7
1.8
1.9
Potential vs. RHE (V)

FIG. 21b

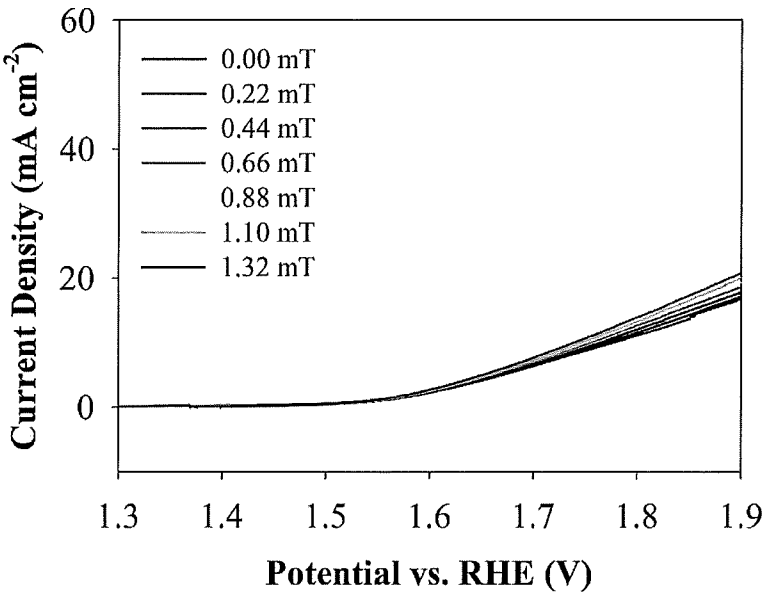
60
40
20
0
Current Density (mA cm-2)
0.00 mT
0.22 mT
0.44 mT
0.66 mT
0.88 mT
1.10 mT
1.32 mT
1.3
1.4
1.5
1.6
1.7
1.8
1.9
Potential vs. RHE (V)

FIG. 22a

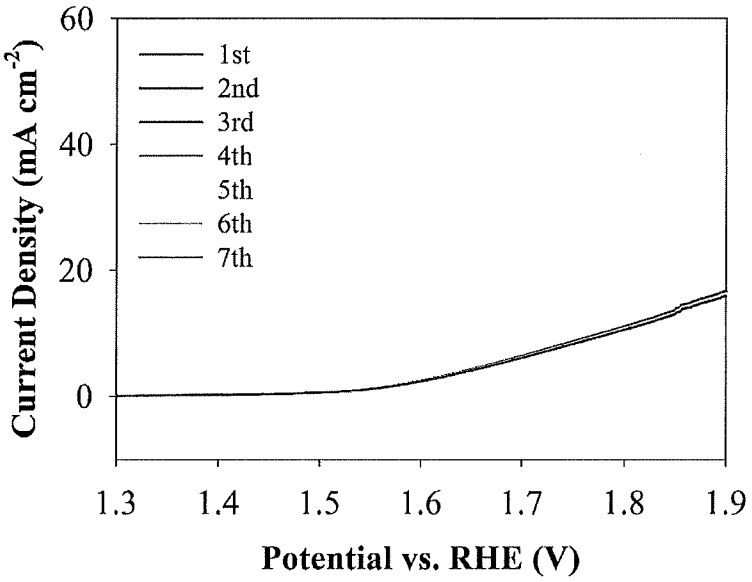
60
40
20
0
Current Density (mA cm-2)
1st
2nd
3rd
4th
5th
6th
7th
1.3
1.4
1.5
1.6
1.7
1.8
1.9
Potential vs. RHE (V)

FIG. 22b

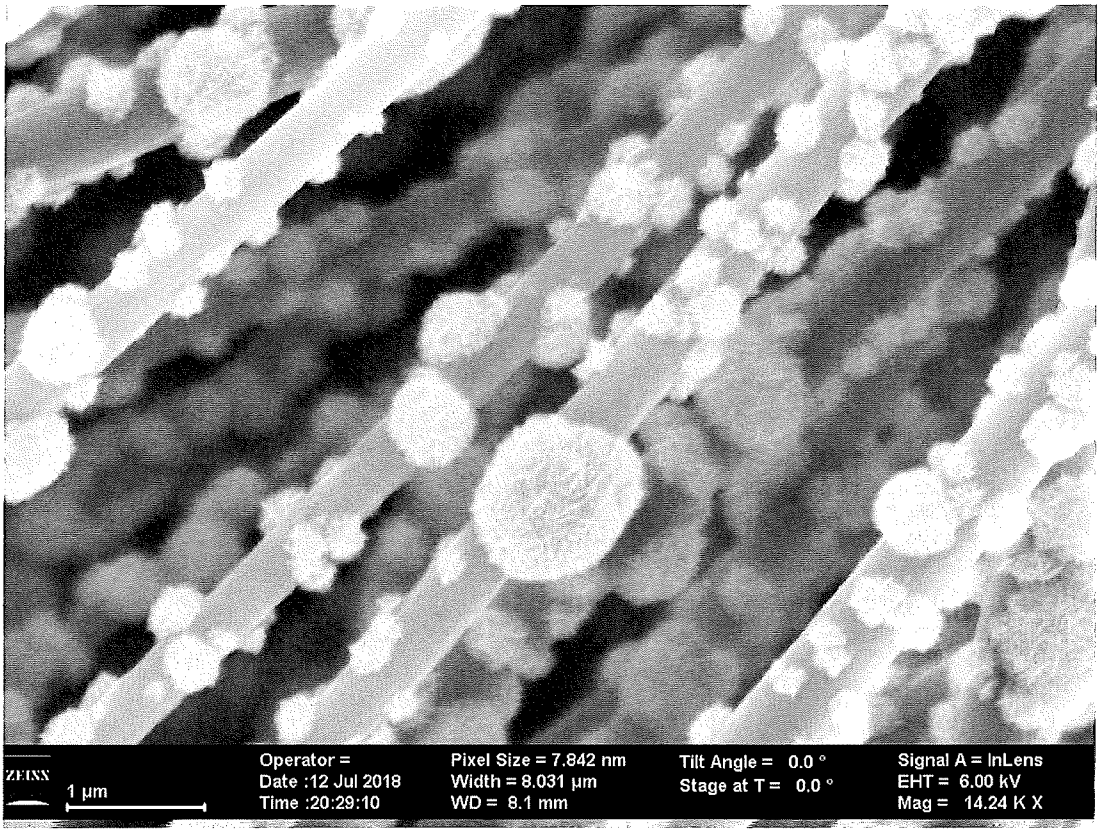
ZEISS
1 µm
Operator =
Date :12 Jul 2018
Time :20:29:10
Pixel Size = 7.842 nm
Width = 8.031 µm
WD = 8.1 mm
Tilt Angle = 0.0 °
Stage at T = 0.0 °
Signal A = InLens
EHT = 6.00 kV
Mag = 14.24 K X

FIG. 23

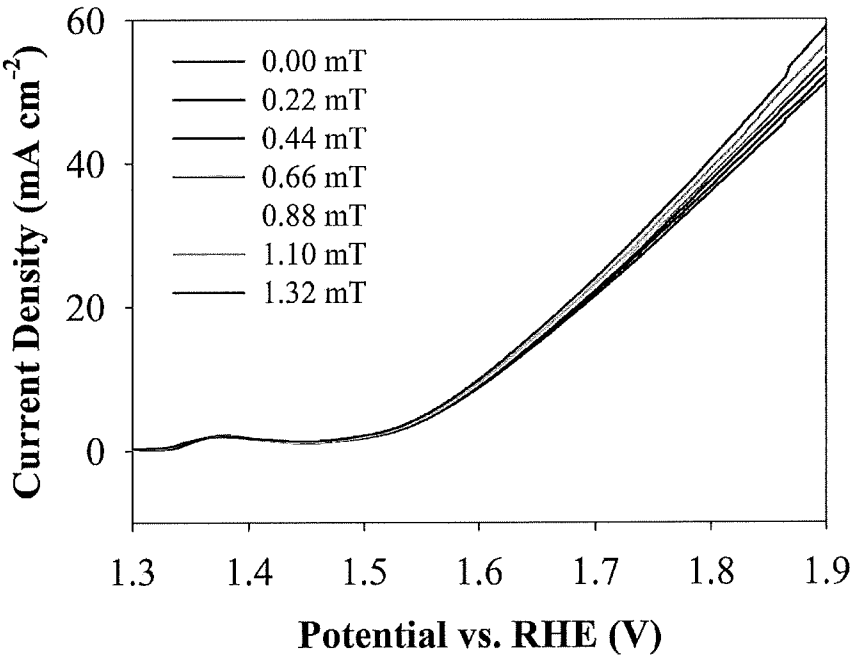
60
40
20
0
Current Density (mA cm-2)
0.00 mT
0.22 mT
0.44 mT
0.66 mT
0.88 mT
1.10 mT
1.32 mT
1.3
1.4
1.5
1.6
1.7
1.8
1.9
Potential vs. RHE (V)

FIG. 24a

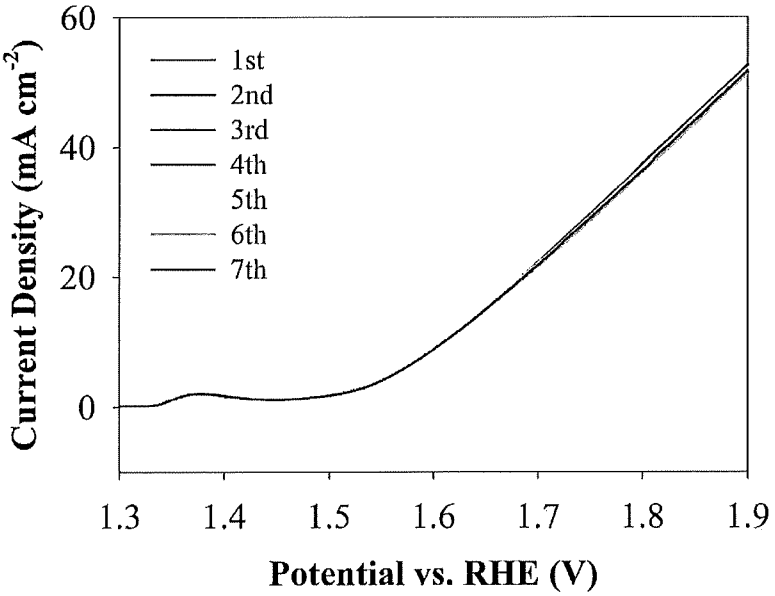
60
40
20
0
Current Density (mA cm-2)
1st
2nd
3rd
4th
5th
6th
7th
1.3
1.4
1.5
1.6
1.7
1.8
1.9
Potential vs. RHE (V)

FIG. 24b

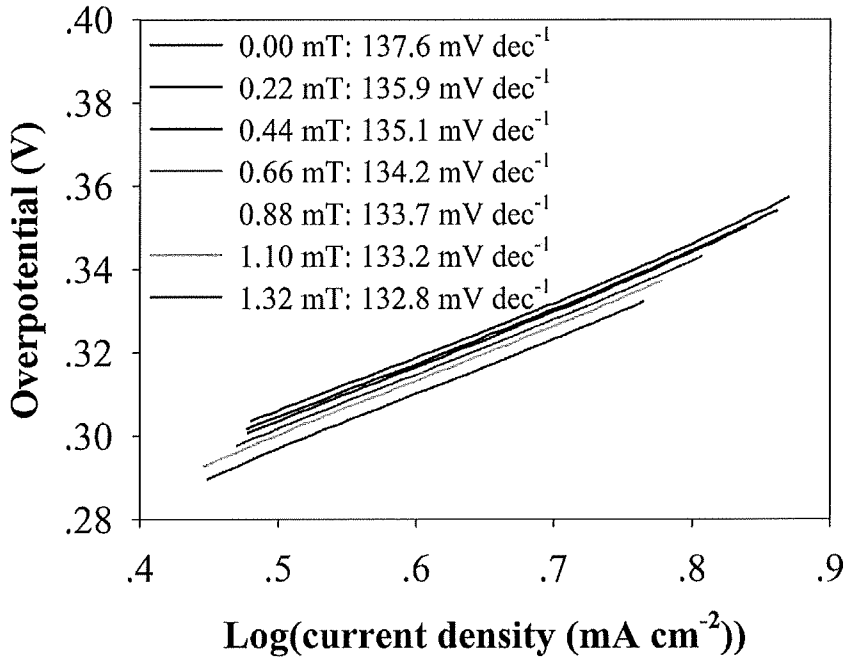
.40
.38
.36
.34
.32
.30
.28
Overpotential (V)
0.00 mT: 137.6 mV dec-1
0.22 mT: 135.9 mV dec-1
0.44 mT: 135.1 mV dec-1
0.66 mT: 134.2 mV dec-1
0.88 mT: 133.7 mV dec-1
1.10 mT: 133.2 mV dec-1
1.32 mT: 132.8 mV dec-1
.4
.5
.6
.7
.8
.9
Log(current density (mA cm-2))

FIG. 24c

INTERNATIONAL SEARCH REPORT

International application No.
PCT/US2019/047675

A. CLASSIFICATION OF SUBJECT MATTER
IPC(8) - C25B 1/02; C25B 11/04 (2019.01)
CPC - C25B 1/02; C25B 11/0405; C25B 11/0415; C25B 11/0452 (2019.08)

According to International Patent Classification (IPC) or to both national classification and IPC

B. FIELDS SEARCHED

Minimum documentation searched (classification system followed by classification symbols)
See Search History document

Documentation searched other than minimum documentation to the extent that such documents are included in the fields searched
USPC - 204/290.1; 204/292 (keyword delimited)

Electronic data base consulted during the international search (name of data base and, where practicable, search terms used)
See Search History document

C. DOCUMENTS CONSIDERED TO BE RELEVANT

Category*	Citation of document, with indication, where appropriate, of the relevant passages	Relevant to claim No.
X --- Y	US 2017/0098843 A1 (BOARD OF REGENTS THE UNIVERSITY OF TEXAS SYSTEM) 06 April 2017 (06.04.2017) entire document	1-7, 10, 11, 13-17 --- 8, 9, 12, 18-33
X --- Y	US 6,207,313 B1 (LEDDY et al) 27 March 2001 (27.03.2001) entire document	34 --- 18-33
Y	US 5,942,349 A (BADWAL et al) 24 August 1999 (24.08.1999) entire document	8, 9, 32, 33
Y	US 9,680,193 B2 (EOS ENERGY STORAGE LLC) 13 June 2017 (13.06.2017) entire document	12
A	US 2013/0306489 A1 (INDUSTRIE DENORA S P A) 21 November 2013 (21.11.2013) entire document	1-34
A	US 2018/0127887 A1 (INDUSTRIE DE NORA S P A) 10 May 2018 (10.05.2018) entire document	1-34
A	WO 2017/182923 A1 (SABIC GLOBAL TECHNOLOGIES B V) 26 October 2017 (26.10.2017) entire document	1-34

☐ Further documents are listed in the continuation of Box C. ☐ See patent family annex.

* Special categories of cited documents:
"A" document defining the general state of the art which is not considered to be of particular relevance
"E" earlier application or patent but published on or after the international filing date
"L" document which may throw doubts on priority claim(s) or which is cited to establish the publication date of another citation or other special reason (as specified)
"O" document referring to an oral disclosure, use, exhibition or other means
"P" document published prior to the international filing date but later than the priority date claimed
"T" later document published after the international filing date or priority date and not in conflict with the application but cited to understand the principle or theory underlying the invention
"X" document of particular relevance; the claimed invention cannot be considered novel or cannot be considered to involve an inventive step when the document is taken alone
"Y" document of particular relevance; the claimed invention cannot be considered to involve an inventive step when the document is combined with one or more other such documents, such combination being obvious to a person skilled in the art
"&" document member of the same patent family

Date of the actual completion of the international search	Date of mailing of the international search report
07 October 2019	29 OCT 2019
Name and mailing address of the ISA/US Mail Stop PCT, Attn: ISA/US, Commissioner for Patents P.O. Box 1450, Alexandria, VA 22313-1450 Facsimile No. 571-273-8300	Authorized officer Blaine R. Copenheaver PCT Helpdesk: 571-272-4300 PCT OSP: 571-272-7774